

Characterisation of SiPMs

R. Klanner*

*Institute for Experimental Physics, University of Hamburg,
Luruper Chaussee 149, D 22761, Hamburg, Germany.*

Abstract

Silicon photomultipliers, thanks to their excellent performance, robustness and relatively simple use, are the photon-detectors of choice for many present and future applications. This paper gives an overview of methods to characterise SiPMs. The different SiPM parameters are introduced and generic setups for their determination presented. Finally, ways to extract the parameters from the measurements are discussed and the results shown. If a parameter can be obtained from different measurements, the results are compared and recommendations given, which is considered to be the most reliable. The characterisation of SiPMs, in particular for high light intensities and in high radiation fields, is presently a field of intensive research with many open questions and problems which will be discussed.

Keywords: Silicon photomultiplier, characterisation, gain, break-down voltage, cross-talk, after-pulse, dark-count rate, non-linearity

Contents

1	Introduction	2
2	SiPM parameters	2
3	Measurement setups	7
3.1	$I - V$ and $C - V$ setup	7
3.2	Current-transient setup	9
3.3	Charge-measurement setup	9
3.4	Absolute PDE setup	10
3.5	Counting methods	12
3.6	Optical observation of Geiger discharges	12
4	Determination of the SiPM parameters	13
4.1	Electrical parameters	13
4.2	Electric field	15
4.3	Breakdown and turnoff voltage	16
4.4	Photon-detection efficiency, number of primary Geiger discharges and gain	19
4.5	Nuisance parameters: Dark-count rate and correlated noise	22
4.6	Non-linearity and saturation	27
5	Conclusions and outlook	30
6	Appendix	32
7	List of References	33

*Email: Robert.Klanner@desy.de, Tel. +49 40 8998 2558.

1. Introduction

In this contribution an overview of different methods of characterising SiPMs is given. After a short discussion of the most relevant parameters and their relation to the electrical parameters of SiPMs, generic measurement setups are presented. Finally, methods how the SiPM parameters can be determined with the different setups are presented, and their advantages, disadvantages and limitations discussed.

Several groups have developed methods of characterising SiPMs and most of them are well documented in publications. As it is not possible to do justice to all this work, only generic setups and analysis methods are presented. One complication is that the different groups use different symbols for the technical terms. In addition, these are not always clearly defined. The next section is an attempt to give clear definitions and to summarise the symbols used in this paper in a table. Clearly a common nomenclature is more than welcome, and efforts towards this goal are important for the advancement of the field [1].

The emphasis of the paper is on the characterisation of Analog SiPMs, on which most of the work has been done so far. This in no way means that the development of Digital SiPMs is not appreciated by the author. In fact the opposite is true, and given the impressive developments of microelectronics and 3-D integration, Digital SiPMs may well surpass in the future Analog SiPMs in many applications.

The paper does not cover the excellent timing performance of SiPMs and its measurements, which however is discussed in other articles of this Special Issue ([2, 3, 4, 5]).

As this is a review paper, most of the results are based on discussions with colleagues or on published papers, for which the sources are quoted. If no reference is given, the results are from measurements by members of the Hamburg Detector Laboratory with the analysis performed by the author. Most of these studies used SiPMs produced by KETEK, as for these devices we have access to the technological information to perform simulations.

2. SiPM parameters

Silicon Photomultipliers, also referred to as SiPM (Silicon photomultiplier or Silicon Photo Multiplier), MPPC (Multi Pixel Photon Counter) or G-APD (Geiger Mode Avalanche Photo Diode, which however is mainly used for single pixel devices) are two dimensional arrays of 100 to several 10 000 single photon avalanche diodes (SPAD), called pixels, with typical dimensions between $10\text{ }\mu\text{m} \times 10\text{ }\mu\text{m}$ and $100\text{ }\mu\text{m} \times 100\text{ }\mu\text{m}$. The pixels are operated in limited Geiger mode and every pixel gives approximately the same signal, independent of the number of photons which have produced simultaneously electron-hole pairs in the amplification region of the pixel. The sum of the pixel signals is proportional to the number of pixels with Geiger discharges, from which the number of incident photons is deduced. As the output charge for a single Geiger discharge is typically larger than 10^5 elementary charges, 0, 1, 2, and more Geiger discharges can be easily distinguished, enabling the detection of single optical photons with high efficiency and sub-nanosecond timing.

Two types of SiPMs have been developed: Analog and Digital. In Analog SiPMs the individual SPADs are connected via quenching resistors to a common readout and the SiPM delivers the summed analog signal. In Digital SiPMs each pixel has its own quenching circuit and a digital switch to a multi-channel readout system. The output is the digitised pulse height and precise time information for the pixels with Geiger discharges. Digital SiPMs also allow disabling pixels with high dark-count rates.

The basic functioning of a SiPM, as well as the terms required for its description are explained with the help of Fig. 1, which shows an example of a possible cross section of a single pixel and the electrical diagram used by the author to simulate the pulses for a SiPM with N_{pix} pixels. More realistic pixel layouts are discussed in Ref. [3]. Different to Fig. 1b, in most of the literature (e.g. Refs. [2, 3, 4]) a voltage source with a value of the break-down voltage is implemented in series with the switch S and the resistance R_d , or more general, the switch S and the resistor R_d are replaced by a time dependent current source. Which of the models is the more appropriate one, is at present an open question.

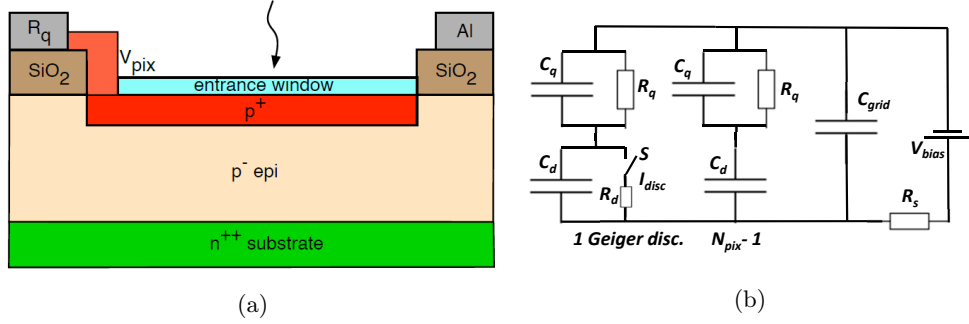


Figure 1: (a) Example of a possible cross section of a single pixel of a SiPM. R_q represents the quenching resistance, and Al the biasing grid. (b) Electrical model for voltages above the breakdown voltage, V_{bd} , of a SiPM with N_{pix} pixels and a single Geiger discharge. $I_{disc}(t)$ represents the discharge current of the pixel by the Geiger discharge, described by a switch and the resistor R_d . $I_{disc}(t)$ can also be simulated by a current source with a time-dependent current. C_{grid} is the capacitance between the Al-grid which connects the individual pixels to the bias voltage and the substrate. The shunt resistor R_s converts the current signal into a voltage, which is sensed by the readout. Most of the simulations found in the literature use a model with a voltage source ($V = V_{bd}$) in series with switch S and the resistor R_d . For an explanation of the other symbols, see text.

The terms used and the corresponding symbols are summarised in Table 1. Fig. 2 shows examples of pulses from single Geiger discharges for a SiPM from KETEK with (a) a pixel size of $25\text{ }\mu\text{m}$, and (b) of $50\text{ }\mu\text{m}$.

Each pixel is connected to the power supply (V_{bias}) by the quenching resistance R_q . Parallel to R_q there is a capacitance C_q . It is the parasitic capacitance of the quenching resistor to the Si-bulk of the pixel and can be intentionally increased to produce a narrow initial pulse allowing a better signal extraction. The capacitance of the diode corresponding to a single pixel is denoted by C_d . R_s is the shunt resistor which converts the current signal into a voltage, which is sensed by the readout. The photon enters the SiPM through a window, which is typically covered by an anti-reflective coating (ARC). The ratio of the area of the entrance window to the pixel area is usually called fill factor, FF .

The SiPM is biased by a voltage V_{OV} above the breakdown voltage V_{bd} : $V_{OV} = V_{bias} - V_{bd}$. In the quiescent state no current flows through R_q and the voltage over the pixel is $V_d = V_{bias}$. An eh (electron hole) pair, produced either thermally, by a photon or by ionising radiation, initiates with the trigger probability P_T a Geiger discharge by avalanche multiplication. P_T is a function of the position where the eh pair is generated. A quantitative model for this dependence is given in Ref. [6]. The discharge takes place through a narrow ($\approx 10\text{ }\mu\text{m}$ diameter) micro-plasma tube until the turn-off voltage V_{off} is reached, when the multiplication is too low to maintain the micro-plasma. In the electrical model shown in Fig. 1b the switch S is closed at the start of the Geiger discharge, C_d is discharged through R_d , and the switch opens when $V_d = V_{off}$. The observed differences $V_{bd} - V_{off}$ are small ($< 1\text{ V}$) and frequently compatible with zero, and in most of the literature just V_{bd} is used. The only paper which reports a significant difference is Ref. [7], and Ref. [8] presents a model calculation of a Geiger discharge and derives a formula for $V_{bd} - V_{off}$. The time constant of the pixel discharge is short compared to 1 ns . It is responsible for the fast rise time of the output pulse seen in Fig. 2b. As discussed in Refs. [9, 10] the decay of the measured pulse has two time constants: a fast one $\tau_{in} \approx R_s \cdot C_{eq}$ and a slower one $\tau_r = R_q \cdot (C_d + C_q)$. τ_r describes the recharging of the pixel after the switch S in Fig. 1b has opened at the end of the Geiger discharge. τ_{in} is associated with the shunt resistance R_s and the total capacitance $C_{eq} \approx N_{pix} (1/C_d + 1/C_q)^{-1}$ seen by the amplifier. The total charge of the SiPM pulse is $Q = (V_{bias} - V_{off}) \cdot (C_d + C_q)$, and the voltage at the peak $V_{max} \approx (Q/C_{eq}) \cdot (C_q/(C_q + C_d))$. The latter formula assumes that the bandwidth of the readout is sufficiently high not to degrade the signal, which is a quite challenging requirement. From Fig. 2 one sees that, contrary to the SiPM with $50\text{ }\mu\text{m}$ pixels, there is no evidence for a fast component for the $25\text{ }\mu\text{m}$ SiPM. It is concluded that in the latter case $C_q \ll C_d$.

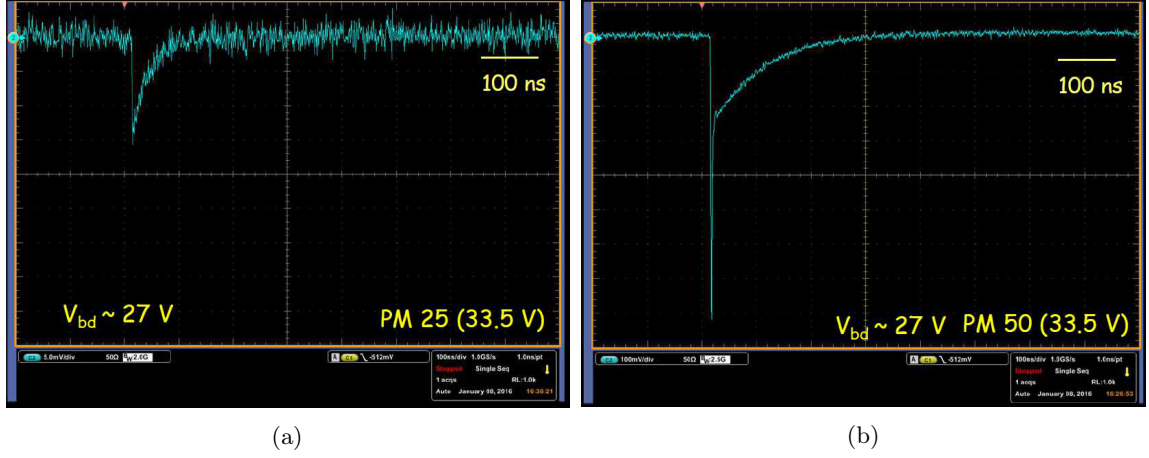


Figure 2: Pulse shape of a single Geiger discharge for (a) KETEK SiPM with 25 μm , and (b) 50 μm pixel size, measured at $V_{bias} = 33.5\text{ V}$ (colour online).

A parameter which is of particular relevance for the characterisation of SiPMs is the gain

$$G = \frac{(C_d + C_q) \cdot (V_{bias} - V_{off})}{q_0} \quad \text{and} \quad G^* = G \cdot f_Q, \quad (1)$$

The elementary charge is denoted q_0 . If the entire signal is integrated, the gain is G . An integration window which is shorter than the pulse or pulse shaping by the readout electronics, result in a gain, G^* , which is reduced by a factor $f_Q \leq 1$.

As shown in Fig. 3, SiPM charge spectra measured in the dark and with low-intensity pulsed light, show peaks which correspond to N_G , the number of pixels with Geiger discharges. The lowest peak corresponds to $N_G = 0$, and the following to $N_G = 1, 2$, etc., with the distance between the peaks $q_0 \cdot G^*$. Following the convention from vacuum photomultipliers, it is customary to show charge spectra in units of photo-electrons (pe), by scaling the Q axis by $1/(q_0 \cdot G^*)$ and shifting the scale so that the $N_G = 0$ peak is at zero. As a result the $N_G = 1, 2, \dots i$ peaks are at $\text{pe} = 1, 2, \dots i$, independent of the value of f_Q . This is also valid if, instead of the charge, the amplitude of the SiPM signal is analysed.

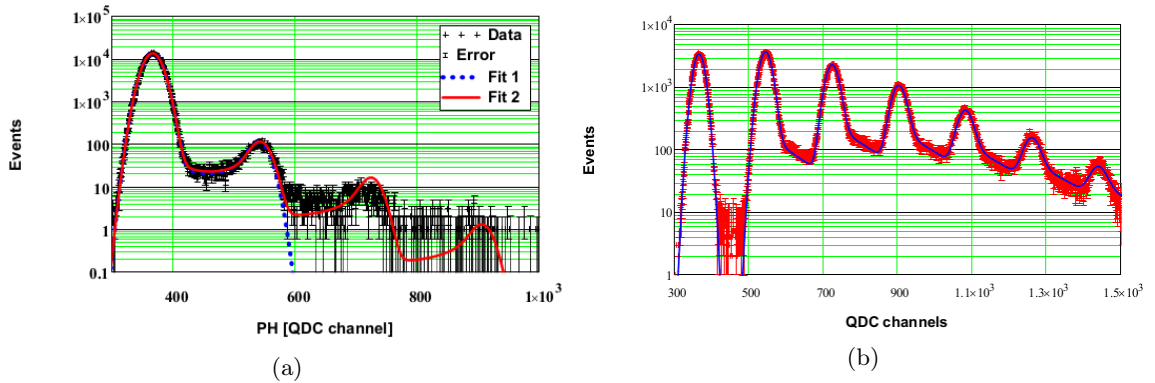


Figure 3: (a) Charge spectra measured using a KETEK SiPM with a pixel size of 15 μm at $V_{bias} = 33\text{ V}$ (a) in the dark, and (b) with sub-nanosecond laser light. The figures are taken from Ref.[11]. In (a), Fit 1 considers only single dark counts randomly distributed in time without correlated noise, whereas for Fit 2 correlated noise and multiple dark counts are included in the model fitted to the data. In (b) the fit function takes into account electronics noise, prompt and delayed correlated noise and gain fluctuations, but not dark counts.

Another important parameter of a photon detector is the photon-detection efficiency, PDE . For a SiPM it is defined as the ratio of primary Geiger discharges due to the photons, $N_{pG, photo}$,

to the number of photons hitting the SiPM, N_γ :

$$PDE = \frac{\langle N_{pG, photo} \rangle}{\langle N_\gamma \rangle} = FF \cdot QE(\lambda) \cdot P_T(V_{bias}, \lambda), \quad (2)$$

where FF is the fill factor (ratio of sensitive area to total area), QE the efficiency of a photon with wavelength λ entering the sensitive SiPM volume and producing an eh pair there, and P_T the probability that the eh pair triggers a Geiger discharge. A primary Geiger discharge can produce correlated secondary Geiger discharges, which can be described by the excess charge factor, ECF , and the excess noise factor, ENF , which are defined below. From the measured mean charge $\langle Q \rangle$, the number of primary Geiger discharges, N_{pG} , can be obtained using:

$$\langle N_{pG} \rangle = \frac{\langle Q \rangle}{q_0 \cdot G^* \cdot ECF}. \quad (3)$$

For an absolute determination of PDE the absolute value of $\langle N_\gamma \rangle$, G^* and ECF have to be known. The relative dependence of $PDE(V_{bias})$ can be obtained more easily from the measured charge spectrum recorded at different V_{bias} values, as discussed in Sect. 4.4.

An ideal photon-detector produces signals with identical shapes linearly scaled with the number photons which have initiated Geiger discharges, and the charge spectrum will consist of δ - functions at 0, 1, 2, ... pe. SiPMs however show a number of differences from an ideal detector, frequently called nuisance parameters. These are:

1. Dark counts produce background signals at the primary dark count rate, DCR .
2. Secondary photons produced during Geiger discharges can generate an electron-hole pair in an adjacent pixel and cause a Geiger discharge there, which results in a double-size signal (d in Fig. 4a). This effect is called prompt cross-talk, and its probability is P_{pCT} .
3. Secondary photons produced in Geiger discharges can generate an electron-hole pair in the non-depleted Si and charge carriers can diffuse into the amplification region of a neighbouring pixel, where they cause a Geiger discharge. This effect is called delayed cross-talk, and its probability is P_{dCT} .
4. During the Geiger discharge, charge carriers can be trapped in defect states and released after some time causing a Geiger discharge in the same pixel as the primary discharge. This effect is called after-pulsing (s+a+a in Fig. 4a). The trapping probability for a state i is called $P_{trap,i}$ and the corresponding time constant $\tau_{trap,i}$. As can be seen from Fig. 4b the signal strength of after-pulses depends on the recovery state of the pixel, and increases proportional to $1 - e^{-t/\tau_r}$. In addition, secondary photons generating electron-hole pairs in the non-depleted Si with charge carriers diffusing into the same pixel as the primary Geiger discharge, contribute to after-pulses. This is called optically-induced after-pulsing.

In addition, pixel-to-pixel gain variations and read-out noise will result in signal fluctuations.

The effects discussed above can also be observed in the charge (Q) spectra recorded with a QDC (Charge-to-Digital-Converter). Fig. 3a shows the charge spectrum for a KETEK SiPM with a pixel size of $15 \mu\text{m}$ at $V_{bias} = 33 \text{ V}$ measured in the dark using a CAEN QDC. The peak around 380 QDC channels corresponds to zero, and the peak at 550 QDC channels to a single Geiger discharge. Double and triple Geiger discharges are also visible. The width of the zero discharge peak is caused by the electronics noise. The single Geiger discharge peak is caused by dark pulses which significantly overlap with the 100 ns gate used for the measurement. The tail to the left of the single discharge peak and the flat part between single and zero peak are due to dark pulses which only partially overlap with the gate. The curve Fit 2 is the result of the fit to the data by a model which includes the nuisance effects enumerated above (Ref. [11]). Fit 1 considers only single dark counts without correlated noise.

Fig. 3b shows the Q spectrum for the same KETEK SiPM illuminated by a sub-nanosecond laser pulse. The laser intensity was tuned to result in approximately 1.3 primary Geiger discharges per pulse. As discussed in Ref. [12], and also observed in the Q spectrum shown, the number of events in the peaks does not follow a Poisson distribution, which is expected for an ideal

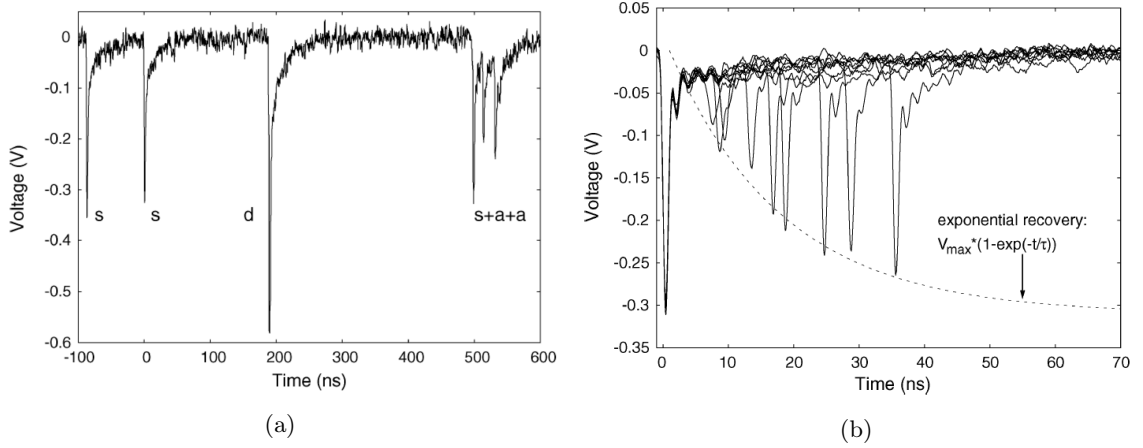


Figure 4: SiPM current transients from Ref. [10] illustrating the different pulse categories mentioned in the text. (a) Single Geiger discharges "s", prompt cross-talk "d", and single discharge with two after-pulses "s+a+a". (b) Transients of after-pulses as a function of time after the initial Geiger discharge. In the figure τ is used for the recovery time τ_r , and V_{\max} for the amplitude of the signal from a single Geiger discharge.

photon-detector if the incoming photons are also Poisson distributed. The observed number of pulses at high Q significantly exceeds the Poisson expectation, which is ascribed to prompt and delayed cross-talk. The statistics of cross-talk, which can be described by a Generalised Poisson distribution, is discussed in detail in Ref. [12]. The events in-between the $N_G = 0$ and the $N_G = 1$ pe peak are again ascribed to dark counts. The events in-between the following peaks and the background below the peaks are ascribed to after-pulses and delayed cross-talk. The shape of the Q spectrum depends on the integration time of the readout electronics, in particular, if only a fraction of the signal is integrated. The curve in Fig. 3b is the model fit described in Ref. [11], which includes effects 2–4, but not 1, which explains the disagreement around channel 450. Note, that fitting separately the peaks with Gauss functions and ignoring the background in-between, which is frequently done, does not give the correct number of Geiger discharges, in particular for high N_G values.

The effect of the nuisance parameters is to change the measured distribution with respect to the distribution of converting photons, which would be the response of the ideal photon detector. Two parameters, the excess charge factor, ECF , and the excess noise factor, ENF , are frequently used to describe the worse performance of a non-ideal detector [13]. They are discussed next. The distribution of photons and the number of primary Geiger discharges, N_{pG} , are assumed to follow a Poisson distribution with the mean $\langle N_{pG} \rangle$ and the root-mean-square (rms) deviation $\sqrt{\langle N_{pG} \rangle}$. The response of the ideal photon-detector will just be the Poisson distribution multiplied with $q_0 \cdot G^*$ resulting in the mean $\langle Q_P \rangle = q_0 \cdot G^* \cdot \langle N_{pG} \rangle$ and the rms deviation $\sigma_P = q_0 \cdot G^* \cdot \sqrt{\langle N_{pG} \rangle}$. If the measured charge distribution of the real photon-detector has the mean $\langle Q \rangle$ and the rms deviation σ_Q for the same number of primary Geiger discharges as the ideal detector, then by definition

$$ECF = \frac{\langle Q \rangle}{\langle Q_P \rangle}, \quad (4)$$

and

$$ENF = \frac{(\sigma_Q / \langle Q \rangle)^2}{(\sigma_P / \langle Q_P \rangle)^2}. \quad (5)$$

As the contribution of the nuisance effects to the measured signal depends on the effective integration time, also G^* , ECF and ENF depend on the readout and the analysis method used, which presents a significant complication. It should also be noted that assuming a Poisson distribution for the photons producing primary Geiger discharges is not necessarily correct for all light sources.

Non-linearity and saturation are other limitations of SiPMs. As the charge from a single pixel is approximately the same for one and more than one simultaneous Geiger discharge, the signal is expected to saturate at $Q_{sat} = N_{pix} \cdot q_0 \cdot G^*$ for high number of photons, N_γ . The saturation can be described by a decrease of the photon-detection efficiency, PDE , because of the already busy pixels. Well below saturation, the mean number of Geiger discharges is approximately given by $PDE_0 \cdot ECF \cdot N_\gamma$, with the photon-detection efficiency without saturation effects PDE_0 . For high numbers of simultaneous photons

$$N_G \approx N_{pix} \cdot (1 - e^{-(PDE_0 \cdot ECF \cdot N_\gamma)/N_{pix}}) \quad (6)$$

is expected because of multiple Geiger discharges in individual pixels. This relation is only valid if the photons are uniformly distributed over the SiPM. If this is not the case, the non-linearity sets in already at lower N_γ values and the functional form is different. If the arrival time of the photons is spread over time, some of the pixels will have already partially recovered when the next photon arrives, and signals exceeding Q_{sat} are expected, and actually observed. The situation is quite complex, however phenomenological parametrisations are available, which describe detailed measurements [14]. High dark count rates, e.g. due to radiation damage, also cause a decrease of PDE due to pixels in the recharging state after Geiger discharges. This topic is addressed in Sect. 4.6 and in the contribution on radiation damage of this Special Issue [15].

For the description of the nonlinearity, the terms *Linearity*, *Nonlinearity* and *Dynamic Range* are frequently used. Note that different definitions are found in the literature. For the linearity, Lin , a minimum and a maximum value of the number of photons to be detected, $N_{\gamma,min}$ and $N_{\gamma,max}$, have to be defined. Then $Lin(N_{\gamma,min}, N_{\gamma,max}) = Res(N_{\gamma,max})/Res(N_{\gamma,min})$, with the *Responsivity* $Res(N_\gamma) = \langle Q(N_\gamma) \rangle / N_\gamma$. The non-linearity is just $NLin = 1 - Lin$. For the dynamic range, values for $NLin$ and for $N_{\gamma,min}$ have to be specified. The ratio of N_γ where the specified $NLin$ is reached to $N_{\gamma,min}$ is defined as the dynamic range. In the situation where zero and one Geiger discharges can be distinguished, $N_{\gamma,min} = 1/PDE_0$ appears to be a reasonable convention.

3. Measurement setups

In this section an overview of different setups used for characterising SiPMs is presented, and some recommendations given.

3.1. $I - V$ and $C - V$ setup

Fig. 5 shows a schematic layout of the measurement setup used for the $I - V$ and $C - V$ measurements. They are best performed on a temperature-controlled chuck in a light tight and electrically shielded box. As it has been observed that SiPM parameters can be influenced by humidity, a humidity measurement and control of the atmosphere in the box is recommended.

For the $I - V$ measurements the ramping of the voltage should be sufficiently slow so that stable conditions at the individual voltage steps are reached. This can be verified by taking $I - V$ data ramping the voltage up and down. For the precise ($\lesssim 10$ mV) determination of the breakdown voltage V_{bd} , a voltage step around V_{bd} of 100 mV is recommended. This small step size should already be used well below V_{bd} (e.g. 3 V), to avoid problems with fitting the data or numerically calculating derivatives. In addition, note that the Keithley voltage source, which is typically used for the measurements, has a setting accuracy of ± 10 mV with a saw-tooth deviation as a function of voltage. This can cause problems for a precise determination of V_{bd} . Last but not least, the possibility to illuminate the SiPM with DC light is highly recommended. For low dark currents, (e.g. at low operating temperatures), this is needed for a precise determination of V_{bd} , and for highly irradiated SiPMs with high pixel occupancies, the comparison of the difference of the current with and without illumination for different radiation fluences can give a first idea on the degradation of the SiPM as photon-detector due to radiation damage (Ref. [15] and Sect. 4.6).

The measurement of the admittance $Y(f)$ as a function of frequency, f , can be used to determine the SiPM electrical parameters. In addition to those already described in Fig. 1b, these are L_s an effective inductance for the biasing lines, and R_I to parameterise the SiPM dark current. Note

Table 1: Parameters and symbols used for the characterisation of SiPMs. The measurement methods are $I_f - V$ and $I_r - V$ for the forward and reverse $I - V$ measurement, *Trans* for the current-transient measurement, and Q for the spectra obtained either by integrating the transients or from the maximum of the pulse of the transient, or from the charge recorded with a charge-to-digital convertor.

Symbol	Parameter	Measurement
V_{bias}	Bias voltage	–
V_{bd}	Breakdown voltage	$I_r - V$
V_{off}	Turnoff voltage	Q
$V_{OV} = V_{bias} - V_{bd}$	Overvoltage	$I_r - V$
I_{dark}	Dark current	$I_r - V$
I_{light}	Current with illumination	$I_r - V$
$I_{photo} = I_{light} - I_{dark}$	Photo current	$I_r - V$
Q	Measured charge (amplitude)	Q
$\langle Q \rangle$	Mean Q	Q
σ_Q^2	Variance of Q	Q
$N_{pix}, (N_{total})$	Number of pixels	–
R_q	Quenching resistance	$I_f - V, C - V$
C_q	Quenching capacitance	$C - V$
$C_d, (C_{pix})$	Pixel capacitance	$C - V, Q$
R_s	Shunt resistor readout	–
I_{disc}	Pixel discharge current	–
R_d	Pixel discharge resistor	–
V_d	Voltage drop over pixel	–
$C_{eq} = N_{pix}(1/C_d + 1/C_q)^{-1}$	Capacitance seen by readout	–
$\tau_{in} = R_s \cdot C_{eq}$	Time const. fast component	<i>Trans</i>
$\tau_r = R_q \cdot (C_d + C_q)$	Recharging time const.	<i>Trans</i>
$G = (V_{bias} - V_{off})(C_d + C_q)/q_0$	SiPM overall gain	<i>Trans, Q</i>
f_Q	Fraction SiPM signal recorded	<i>Trans, Q</i>
$G^* = G \cdot f_Q$	Measured gain	Q
N_γ	Number of photons on SiPM	–
$PDE = FF \cdot QE \cdot P_T$	Photon-detection efficiency	$Q, Trans$
PDE_0	<i>PDE</i> in linear range (low N_γ)	$Q, Trans$
FF	Fill factor	–
QE	Quantum efficiency	–
P_T	Geiger breakdown probability	–
$P_{T, photo}$	P_T for photons	–
N_G	Number Geiger discharges	Q
N_{pG}	Number primary Geiger discharges	Q
$N_{pG, photo}$	N_{pG} due to photons	Q
pe	Unit <i>Geiger discharges, (photo-electrons)</i>	<i>Trans, Q</i>
f_0	Fraction events in $N_G = 0$ peak	Q
$f_{0, dark}$	f_0 in the dark	Q
$f_{0, light}$	f_0 with light	Q
$f_{0.5}$	Fraction events above 0.5 pe	Q
$f_{1.5}$	Fraction events above 1.5 pe	Q
DCR	Dark count rate	$I_r - V, Q, Trans$
DCR_p	Primary <i>DCR</i>	$I_r - V, Q, Trans$
P_{pCT}	Probability prompt cross-talk	$Q, Trans$
P_{dCT}	Probability delayed cross-talk	$Q, Trans$
P_{AP}	After-pulse probability	$Q, Trans$
ECF	Excess charge factor	Q
ENF	Excess noise factor	Q
Lin	Linearity	Q
$NLin = 1 - Lin$	Non-linearity	Q
DR	Dynamic range	Q
$Res = \langle Q(N_\gamma) \rangle / N_\gamma$	Responsivity	Q

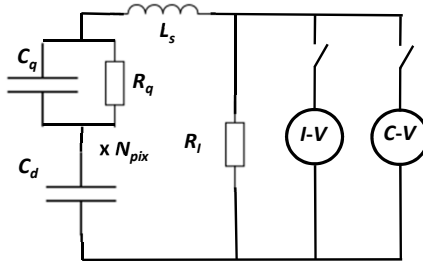


Figure 5: Generic setup for the $I - V$ and $C - V$ measurements. The elements used to analyse the measurements in addition to the ones already shown in Fig. 1b are the parasitic elements L_s , and R_I for the dark current. Their meaning is described in the text. The grid capacitance, C_{grid} , shown in Fig. 1b has not been implemented in the analysis.

that in this model the capacitance of the voltage distribution grid in parallel to R_I , discussed e.g. in Refs. [16, 17], is not included. As will be shown in Sect. 4.1 this model gives a fair description of the measured data. For the measurements a large frequency range, e.g. $f = 100 \text{ Hz}$ to 2 MHz should be chosen with about 3 f -values per decade. High frequencies are in particular relevant for the determination of C_q . Only at high frequencies a significant fraction of the AC-current flows through C_q and its effect can be seen in the $Y - f$ measurements. Experience has shown that a value of V_{bias} between 0.5 and 1 V below V_{bd} gives reliable results, even if the dark-count rate is very high ($> 1 \text{ GHz}$). As discussed in Sect. 4.2, $C - V$ measurements can be used to estimate the doping profile and the electric field of the avalanche region.

3.2. Current-transient setup

A number of groups (e.g. [13, 18, 19]) are using setups to characterise SiPMs by recording the current transients. They all follow a similar design: The SiPM is mounted in a temperature-controlled chamber, where it can be uniformly illuminated by a sub-nanosecond pulsed light source. The SiPM signal is amplified by a low-noise high-bandwidth amplifier and the waveform digitised by a digital oscilloscope or digitiser. A PC is used for steering the measurements, for storing the data and for performing a first on-line analysis. Fig. 6 shows the setup at FBK as an example. Details can be found in Ref. [13]. Together with this setup a complete analysis chain has been developed which allows a fast and reliable characterisation of large samples of SiPMs. It should be noted that, if such a setup is used to investigate highly-irradiated SiPMs where the dark current can exceed tens of mA, the heating of the SiPM is significant and the exact knowledge of the SiPM temperature is quite a challenge. In addition, the voltage drop over the protection, filter and readout resistors has to be taken into account. Such effects can be investigated using a non-irradiated SiPM and simulating the high DCR by an additional DC light source. To the author's knowledge, such a study has so far not been reported.

The recording of the transient allows for a most complete characterisation of SiPMs: In the off-line data analysis, pulse amplitudes and time delays of pulses correlated with the primary discharges can be investigated, as well as charge and amplitude distributions for different pulse integration times and digital pulse shaping evaluated. However, the effort to set up a system with low noise, high performance and precise temperature control is significant and requires quite some expertise.

3.3. Charge-measurement setup

Recording charge spectra from SiPMs is significantly simpler than recording and analysing current transients. However, the time information, required for a detailed understanding of the nuisance parameters, is not available. Again a number of groups (e.g. [20, 21, 22, 23, 24]) have set up such systems. An example from Ref. [23] is shown in Fig. 7. A pulse generator triggers a LED, which illuminates the SiPM. The SiPM signal is amplified by a factor 50 (for a 50Ω load) by

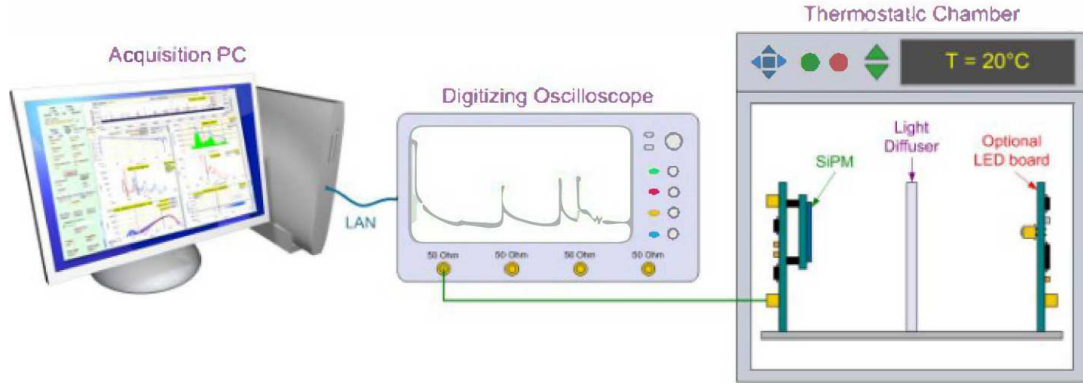


Figure 6: Setup from Ref. [13] for the characterisation of SiPMs using a digital scope for transient recording. It consists of a climate-controlled chamber, the SiPM with its amplifier, a digital scope with a sampling rate of 10 GS/s and a bandwidth set to 500 MHz and a PC for data acquisition.

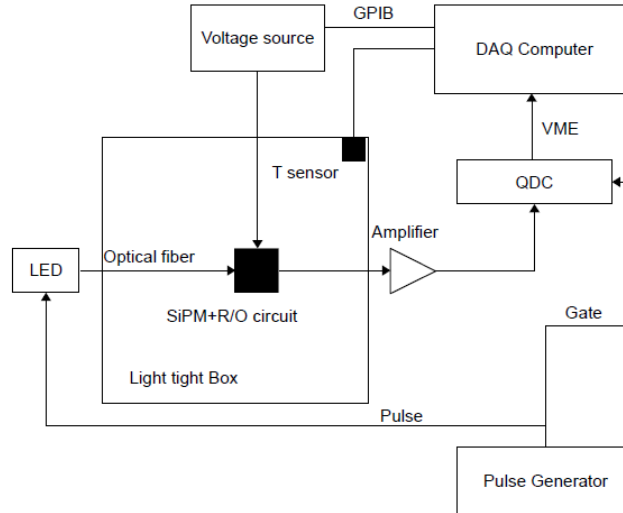


Figure 7: Schematic diagram of the setup from Ref. [23] for the characterisation of SiPMs recording charge spectra.

a high-bandwidth amplifier and recorded by a Charge-to-Digital-Convertor (QDC) with the gate generated by the pulse generator.

In addition to home-built systems, several firms offer SiPM evaluation kits. An example is the *SiPM Educational Kit* from CAEN [24]. A photo of such a setup is shown in Fig. 8. It consists of a LED emitting light of 400 nm with sub-nanosecond rise time and 5 ns decay time, a two-channel power supply-amplifier unit and a two-channel 250 MS/s digitiser with 12 bit dynamic range. The firmware allows charge integration, pulse-shape discrimination and triggering. In this way high-speed recording of charge spectra is possible. Commercial and custom built systems, which record charge spectra, are particularly well suited for the high-throughput characterisation of SiPMs.

3.4. Absolute PDE setup

For measuring the photon-detection efficiency, *PDE*, the response of the SiPM is compared to the response of a calibrated photo-detector. Both pulsed and DC measurements, or a combination of both are used. Again, several setups (e.g. [13, 19, 21, 25, 26, 27]) following similar concepts are in use. As an example, the layout from Ref. [21] is shown in Fig. 9.



Figure 8: CAEN setup (Ref. [24]) for the characterisation of SiPMs. It is a modular plug-and-play system which is simple to set up and allows characterising many properties of SiPMs. A suite of analysis software comes with the system. Similar systems are also available from other vendors. These systems are ideal for a first step towards characterising SiPMs and also well suited for laboratories for pupils and students.

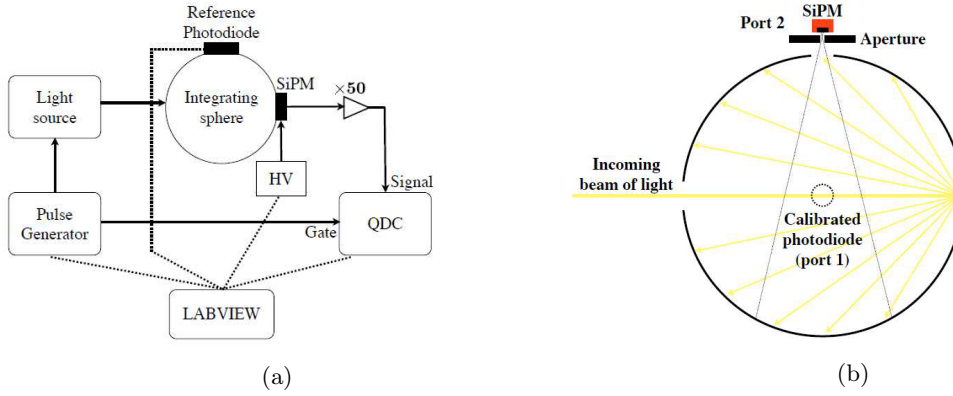


Figure 9: (a) Schematic layout of the PDE measurement from Ref. [21]. The absolute normalisation is obtained by measuring the power of the light source with a calibrated photo-diode. (b) Sketch of the integrating sphere and the positions of the SiPM and the calibrated photo-diode. The angles between the individual openings are 90° .

As light sources pulsed laser diodes and LEDs with pulse widths below 2 ns are used. The wavelength spectra have a FWHM of typically 5 nm for the laser and 10 to 20 nm for the LED. The SiPM output signal is amplified by a fast amplifier and digitised by a QDC with an integration gate of 50 to a few 100 ns depending on the SiPM pulse shape. Dark spectra and spectra with pulsed light are recorded. The light intensity is adjusted so that the fraction of events without a SiPM pulse, $f_{0,light}$, can be determined precisely. Assuming Poisson statistics for the number of dark counts and of primary Geiger discharges, the mean number of primary Geiger discharges per pulse from the photons of the light source is

$$\langle N_{pG,photo} \rangle = \ln(f_{0,dark}/f_{0,light}), \quad (7)$$

with $f_{0,dark}$ the fraction of events without a SiPM pulse under dark conditions. When deriving this formula the fact is used that in the absence of a Geiger discharge, there are no correlated pulses, and the mean number of primary discharges $\langle N_{pG} \rangle$ for both light and dark condition is obtained from the zero probability of the Poisson distribution: $P(0, \langle N_{pG} \rangle) = e^{-\langle N_{pG} \rangle}$. Finally, the absolute PDE is obtained by normalising to the power P_{ref} measured by the calibrated reference diode and $PR_{1/2}$, the measured power ratio of port 1 to port 2 using

$$PDE = \frac{\langle N_{pG,photo} \rangle \cdot PR_{1/2} \cdot f_{Laser}}{P_{ref}/(h\nu)}, \quad (8)$$

with the laser repetition rate f_{Laser} and the photon energy $h\nu$.

The PDE for typically four wavelengths is determined as described above. In order to extend the measurements to wavelengths in the range between 300 and 1000 nm, a Xe lamp with a monochromator is used as light source and the current from the SiPM and the reference diode is measured. As the current includes cross-talk and after-pulses, the measurements have to be normalised to the PDE measurements described above. With a careful control of different systematic effects, absolute PDE values with an $\approx 3\%$ uncertainty for wavelengths between 350 and 800 nm have been determined [19]. For lower wavelengths the uncertainties are dominated by stray light, and above 800 nm by the knowledge of the quantum efficiency of the Si reference diode. In Ref. [28] a precision method with two integrating light spheres is presented. In Ref. [29] a double attenuator techniques is described which achieves an absolute uncertainty below 0.5 % at a wavelength of 770 nm.

3.5. Counting methods

An elegant method for a quick determination of the nuisance parameters DCR and correlated noise, is described in Ref. [21]. The schematic layout is shown in Fig. 10a.

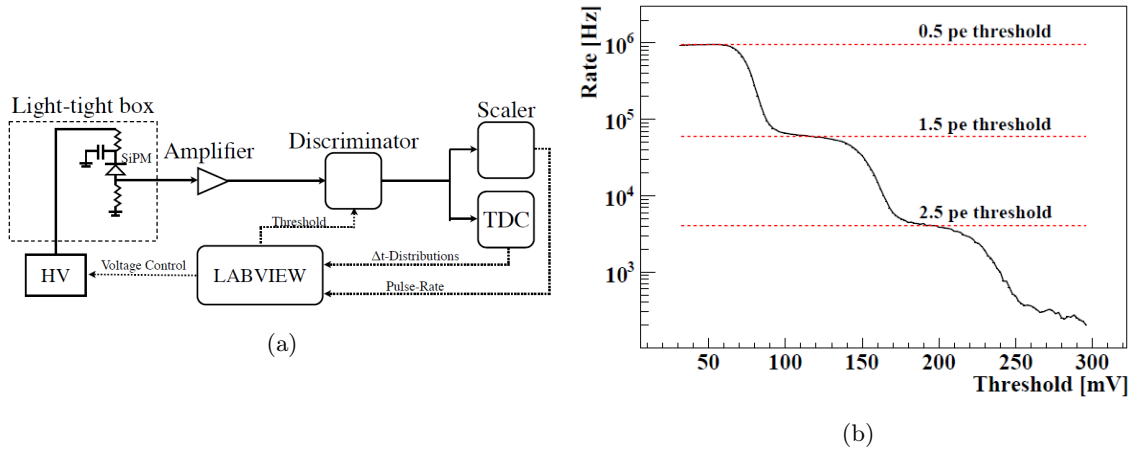


Figure 10: (a) Setup from Ref. [21] for the DCR , cross-talk and after-pulse measurements. For the DCR and cross-talk measurement the count rate as function of discriminator threshold is measured; for the after-pulse measurement the discriminator output is connected to the TDC. (b) Measured count rate as function of discriminator threshold. The unit pe corresponds to the amplitude of a single Geiger discharge.

The measurements are performed in the dark. Fig. 10b shows the count rate as function of the discriminator threshold in units of pe, the amplitude of a single Geiger discharge. The curve, which corresponds to the cumulative pulse-amplitude distribution, shows characteristic plateaus at 0.5, 1.5, and 2.5 pe. The rate $Rate_{0.5}$ for 0.5 pe gives the DCR , and the ratio $Rate_{1.5}/Rate_{0.5}$ approximately the overall cross-talk probability.

For the measurement of the time dependence of the delayed correlated pulses, the discriminator threshold is set to a value well above the electronics noise and the time between triggers is measured using the TDC. The measured time distribution can be fitted by the sum of delayed pulses with two time constants and the dark-count contribution. More details are given in [21] noting that the functions used for the fits (Eq. 5 and 6 in the Ref.) are only approximately correct. A similar analysis with an improved formula is given in Ref. [30].

It should be noted that this and more information can be obtained from the Δt method using current transients as described in Sect. 3.2, which is probably the reason why the counting method is not widely used.

3.6. Optical observation of Geiger discharges

To study the spatial distribution and extension of Geiger discharges, the author of Ref. [31] uses the setup shown in Fig. 11a. The method is based on the observation that Geiger discharges emit

optical and near-infrared photons, as first shown in Ref. [32] and studied quantitatively in Ref. [33]. In Ref. [34] the light spectrum from a Hamamatsu SiPM has been measured in the wavelength range between 450 and 1600 nm.

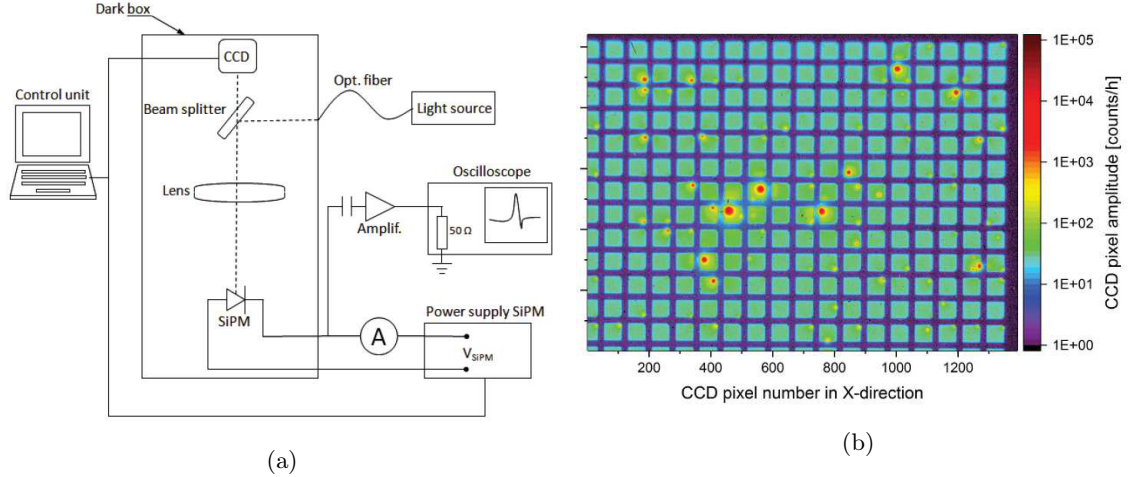


Figure 11: (a) Setup from Ref. [31] to study the light emission from Geiger discharges in SiPMs. (b) Distribution of the observed light intensity from Geiger discharges for a KETEK SiPM with a pixel size of $50\text{ }\mu\text{m}$.

In Ref. [31] the SiPM is imaged by a high resolution CCD camera with a sensitivity for photons between 300 and 900 nm. Fig. 11b shows the image of a KETEK PM3350T SiPM ($50\text{ }\mu\text{m}$ pixels) in the dark at 20°C for $V_{OV} = 5.4\text{ V}$ and an exposure time of 4 h. Assuming that on average every Geiger discharge produces the same amount of light, the observed light intensity is proportional to DCR . Hot-spots are observed with a light intensity approximately 20 times higher than the average. These high generation rates are explained by the presence of point defects, either of the starting material or generated during the fabrication process. A similar observation has been made in Ref. [35] using a digital SiPM, where individual pixels can be disabled and the DCR of individual pixels measured. Thus, the frequently made assumption, that the distribution of dark counts can be described by a Poisson distribution with the same mean for every pixel, is in strong disagreement with this observation. It may be a better approximation for highly radiation-damaged SiPMs. This however has not yet been demonstrated.

Fig. 11b also shows that the hot-spots are fixed in space and that the light spots have a diameter of about $10\text{ }\mu\text{m}$, much smaller than the $50\text{ }\mu\text{m}$ pixel size, which allows estimating the diameter of the micro-discharge channels. It is also reported that the diameter of the light spots does not depend on V_{OV} .

4. Determination of the SiPM parameters

In the following, it is described how the different parameters discussed in Sect. 2 can be determined using the setups presented in Sect. 3. Most of the parameters can be determined in several ways. Some comments will be given, which way the author considers to be the most trustworthy. As discussed in Ref. [15], most of the methods cannot be applied if the DCR or the noise is so high that 0, 1, and more Geiger discharges cannot be distinguished. Ideas on how to characterise SiPMs in these situations will be presented.

4.1. Electrical parameters

To illustrate the determination of the electrical parameters, results are presented for 4 different KETEK SiPMs studied in Ref. [7]. Their names and parameters are given in Table 2. They all have an area of 1 mm^2 , PNCV is a special, single pixel produced by KETEK for testing purposes.

	PM15	PM25	PM50	PM100	PNCV
N_{pix}	4384	1600	400	100	1
$pitch$	15 μm	25 μm	50 μm	100 μm	1 mm
C_d	18 fF	69 fF	330 fF	1.5 pF	110 pF
R_q	750 k Ω	500 k Ω	340 k Ω	410 k Ω	130 Ω
C_q	< 5 fF	< 10 fF	25 fF	155 fF	–
R_I	85 G Ω	80 G Ω	70 G Ω	50 G Ω	85 G Ω
τ_r	14 ns	25 ns	100 ns	620 ns	14 ns

Table 2: Geometrical parameters (top) and electrical parameters as determined from the admittance-frequency ($Y - f$) measurements (bottom) of the KETEK SiPMs investigated.

It cannot be used as photo-detector for voltages above V_{bd} , because the value of R_q is too low to quench the Geiger discharge.

The admittance-frequency, $Y - f$, measurements were performed at 0.5 and 1 V below the breakdown voltage for 27 frequencies between 100 Hz and 2 GHz. The LCR-meter used records

$$Y(f) = 1/R_{par}(f) + i\omega \cdot C_{par}(f), \quad (9)$$

with the parallel resistance, R_{par} , and the parallel capacitance, C_{par} . The series capacitance, C_{ser} , and the series resistance, R_{ser} , are obtained from Eq. 9 using $Z(f) = 1/Y(f) = R_{ser} + 1/(i\omega \cdot C_{ser})$. For the analysis, the electrical model shown in Fig. 5 with the $C - V$ switch closed, is used. The admittance of a single pixel is given by

$$Y_{pix} = \left(\left(\frac{1}{R_q} + i\omega \cdot C_q \right)^{-1} + \frac{1}{i\omega \cdot C_d} \right)^{-1}, \quad (10)$$

and the total admittance by

$$Y_{tot} = \left((N_{pix} \cdot Y_{pix})^{-1} + i\omega \cdot L_s \right)^{-1} + \frac{1}{R_I}. \quad (11)$$

Fig. 12 shows as a function of frequency the measured C_{par} and R_{ser} . From Eq. 11 follows that for intermediate frequencies $C_{par} \approx N_{pix} \cdot C_d$, and at high frequencies, for $\omega \cdot C_q \gg 1/R_q$, $C_{par} \approx N_{pix} \cdot (1/C_q + 1/C_d)^{-1}$. For the SiPMs PM50 and PM100, where a significant fast component is observed in the current transient (see Fig. 2), the decrease of C_{par} at high frequencies can be seen in Fig. 12a. At high frequencies, the dominant contribution to $Z_{tot} = 1/Y_{tot}$ is R_q/N_{pix} in series with $N_{pix} \cdot C_d$. Thus in Fig. 12b at high frequencies the constant value of $R_{ser} \approx R_q/N_{pix}$ gives an approximate value of R_q . With these initial values for C_d , C_q , and R_q , all 5 parameters of the model (C_d , C_q , R_q , L_s , R_I) are adjusted until the data are well described. The results are shown as solid lines in Fig. 12.

It is concluded that the electrical SiPM parameters can be approximately determined from $Y - f$ measurements and that with this method the change of these parameters with irradiation can be determined for highly irradiated SiPMs, where dark-count rates exceed GHz. Ref. [36] reports such a study for radiation damage by X-rays, and Ref. [37] by reactor neutrons up to fluences of $5 \times 10^{14} \text{ cm}^{-2}$. A detailed study of the accuracy of this method and its dependence on the SiPM design has so far not been published. However, it is surprising that this method of determining the electrical SiPM parameters is hardly used.

The standard way of determining R_q is to measure the current for forward bias with a setup as shown in Fig. 5 with the $I - V$ switch closed. For sufficiently high V_{bias} values the diode becomes conductive and the differential resistance is $1/(dI_f/dV_{bias}) \approx R_q/N_{pix}$. Examples for such measurements from Ref. [19] are shown in Fig. 13.

Fig. 13a shows the $I_f - V$ results for temperatures between -40° and $+40^\circ \text{C}$ with straight-line fits for $V_{bias} > 2 \text{ V}$. The inverse of the slope gives R_q/N_{pix} . Fig. 13b shows the temperature dependence of R_q . As expected for a poly-Si resistor, the resistance increases with decreasing temperature.

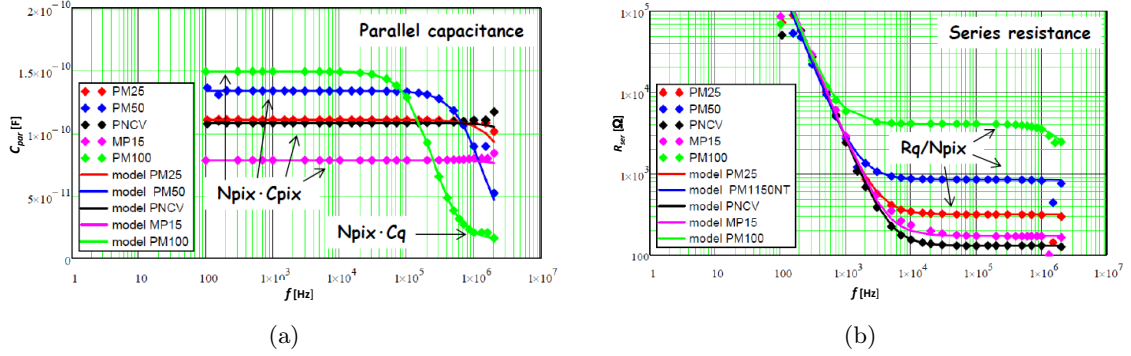


Figure 12: Analysis of the admittance-frequency ($Y - f$) measurements for KETEK SiPMs with different pixel sizes measured 0.5 V below the breakdown voltage, $V_{bd} \approx 27.5\text{ V}$, and 20°C . From the $Y - f$ data (a) the parallel capacitance, C_{par} , and (b) the series resistance, R_{ser} , as a function of frequency are shown. As discussed in the text, approximate values of the electrical parameters C_d (C_{pix} in the figure) and R_q can be obtained directly from the values of constant C_{par} and R_{ser} .

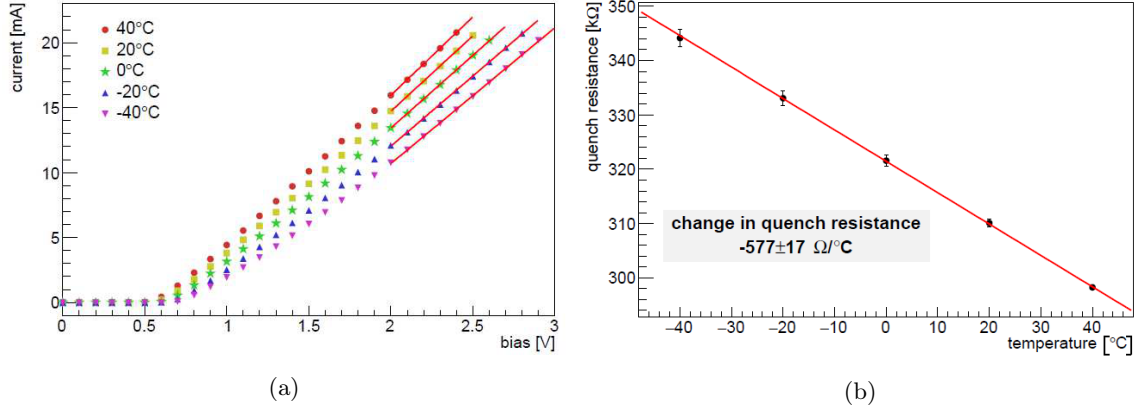


Figure 13: Determination of the quenching resistance, R_q , from the $I_f - V$ measurement for different temperatures with forward bias for the Hamamatsu S13360-3050CS SiPM from Ref. [19]. (a) The value of R_q is obtained from a linear fit to the $I_f - V$ measurement for $V_{bias} > 2\text{ V}$. (b) The value of R_q as function of temperature.

From the author's experience, the value obtained for R_q depends on the fit range, and the derivative dI_f/dV_{bias} approaches, but does not reach a constant value. For the KETEK SiPMs studied by the author, the value of R_q from the $I_f - V$ measurement is typically 5% higher than the one found from the $Y - f$ measurements, which is assumed to be more accurate. However, for the SiPM characterisation the precise knowledge of R_q is not so important.

4.2. Electric field

From $C - V$ measurements it is possible to estimate the doping density and the electric field in the amplification region. Such information, which is only rarely communicated by the vendor to the user, is required to simulate the Geiger breakdown probability as a function of position, which can be done using the formulae given in Ref. [6]. For the determination of the electric field the standard 1-D textbook formulae for an asymmetric pn junction given e.g. in Ref. [38] can be used:

$$x(V_{bias}) = \frac{\varepsilon_0 \varepsilon_{Si} A}{C(V_{bias})} \quad \text{and} \quad N_d(x) = \frac{2}{q_0 \varepsilon_0 \varepsilon_{Si} A^2} \cdot \frac{1}{d(1/C)^2/dV_{bias}} \quad (12)$$

with the distance from the pn junction x , and the doping density $N_d(x)$, and

$$E(x) = \int_{x_{max}}^x \frac{q_0 N_d(x)}{\varepsilon_0 \varepsilon_{Si}} dx \quad (13)$$

for the electric field $E(x)$. The SiPM area is denoted by $A = N_{pix} \cdot pitch^2$, the elementary charge by q_0 and the dielectric constant of Si by $\epsilon_0 \epsilon_{Si}$. The maximal depletion depth reached is $x_{max} = x(V_{bias, max})$, where $V_{bias, max} = 27$ V is the maximum bias voltage used in the measurements. Fig. 14 shows the results for the KETEK SiPMs of Table 2. For these SiPMs the pn junction is close to the entrance window, the built-in depletion depth is about $0.35 \mu\text{m}$, and the maximal electric field ≈ 350 kV/cm for V_{bias} approximately 0.5 V below the breakdown voltage V_{bd} . The full depletion depth is about $1 \mu\text{m}$, which is quite shallow, and results in a relatively narrow amplification region. The observation, that the electric field obtained for the PNCV, a single 1 mm^2 diode, and for the SiPMs with different pixel sizes are approximately the same, confirms that assuming the 1-D model and taking the entire SiPM area for A in the analysis, are reasonable for the SiPM investigated. The electric field above V_{bd} can be estimated, by adding $(V_{bias} - V_{bias, max})/x_{max}$ to the field determined below V_{bd} .

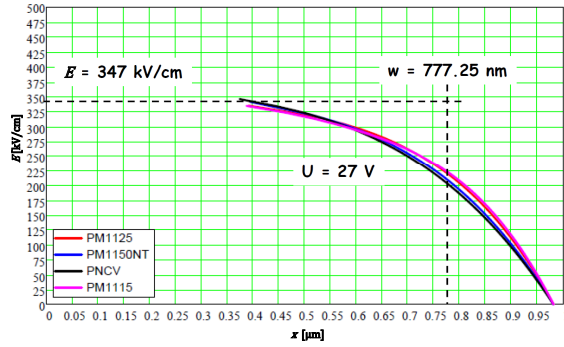


Figure 14: Electric field as a function of the distance from the pn junction determined from $C - V$ measurements in the range $V_{bias} = 1$ to 27 V for the SiPMs listed in Table 2.

4.3. Breakdown and turnoff voltage

Consistent with the discussion in Sect. 2, a distinction is made in this paper between V_{bd} , the voltage at which Geiger discharges start to occur, and V_{off} , the voltage at which the Geiger discharges are quenched. In Ref. [7] a difference $V_{bd} - V_{off}$ of about 1 V is reported for a specific SiPM, and in Ref. [8] a model calculation for $V_{bd} - V_{off}$ is presented. However, in most of the literature only V_{bd} is used, and this issue still has to be clarified. If the SiPM is operated well above V_{bd} , a small difference $V_{bd} - V_{off}$ has only a small effect. However, if the SiPM is operated close to V_{bd} , which may be required at high dark count rates due to background light or radiation damage, the effect could be significant.

Two types of measurements are used to determine the breakdown voltage V_{bd} : Analysis of the $I - V$ characteristics and extrapolation of $PDE(V_{bias})$ to $PDE(V_{bd}) = 0$. For the determination of the turn-off voltage V_{off} , the linear gain-voltage dependence, $G^*(V_{bias})$ is extrapolated to $G^*(V_{off}) = 1$.

Fig. 15 shows $I - V$ measurements for the KETEK SiPM MP15 at $+20^\circ\text{C}$ and -20°C in the dark and with DC illumination by a blue LED with low and high photon intensity. The current scale extends over 9 orders of magnitude. At V_{bd} the currents with and without illumination increase rapidly due to the onset of Geiger discharges. As will be shown later quantitatively, at a given temperature the same V_{bd} value is observed with and without illumination. Between $+20^\circ\text{C}$ and -20°C V_{bd} decreases by ≈ 900 mV, because of the increase of the charge-carrier ionisation coefficients with decreasing temperature.

Below V_{bd} the $I - V$ characteristics are very different for the data with and without illumination: With illumination (I_{light}) the expected increase in current due to avalanche multiplication – the regime in which Avalanche Photo-Diodes (APDs) are operated – is observed, whereas without illumination (I_{dark}) the current is constant up to V_{bd} . The reason is that I_{dark} below V_{bd} is dominated by surface-generation current from the depleted Si-SiO₂ interface, which misses the amplification region and is therefore not amplified.

At V_{bd} the current rises rapidly, with an increase which is higher for the illuminated SiPM. The reason is again that charge carriers from the Si-SiO₂ interface bypass the amplification region. It is also seen that the relative slope of I_{dark} is steeper than of I_{light} above V_{bd} . The reason is the position dependence of the Geiger trigger probability, P_T . It is highest close to the pn junction, which for this SiPM is located near to the SiPM entrance window. Whereas the thermally generated eh pairs are approximately uniformly generated in the depletion region, the blue light has an absorption length of $\approx 0.1\mu\text{m}$ and generates eh pairs in the region of highest P_T only. With increasing V_{bias} the region of high P_T extends further and further into the amplification region, thus increasing $\langle P_T \rangle$ for the uniformly generated eh pairs from dark counts.

At voltages above $V_{bias} \approx 37\text{ V}$, I_{dark} and I_{light} at -20°C show an increase of the slope of $\ln(I)$ compared to the $+20^\circ\text{C}$ data. It still has to be investigated if this increase is due to Geiger discharges for which the quenching is delayed and the current through R_q during the discharge contributes significantly to the signal, or to an increased correlated noise (e.g. after-pulses) at high electric fields and low temperature.

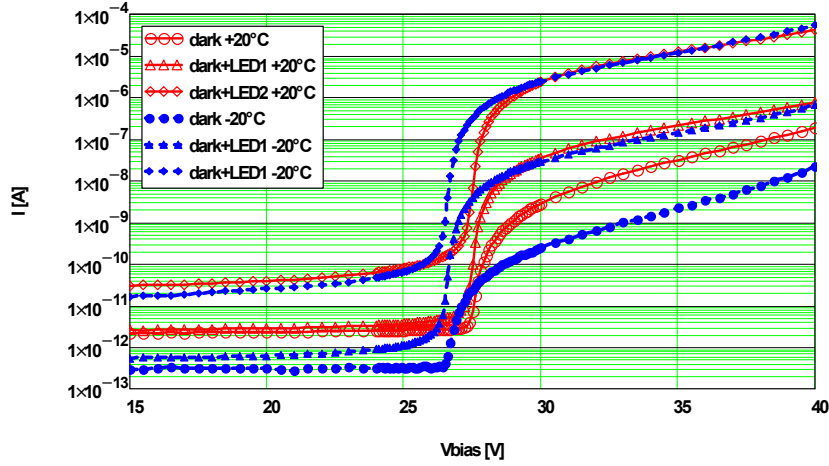


Figure 15: Current versus V_{bias} for the KETEK SiPM measured at $+20^\circ\text{C}$ and -20°C in the dark ("dark") and with DC-illumination by a blue LED with low ("dark+LED1") and high ("dark+LED2") intensity. After subtracting the dark current, the photo-currents for LED1 and LED2 scale (not shown).

Several methods are used to determine V_{bd} from the $I(V_{bias})$ measurements giving all similar results, and it is a matter of taste which one to use. Most of them use either the logarithmic derivative, $LD = d\ln(I)/dV_{bias}$, or its inverse $ILD = 1/LD$. The advantage of LD and ILD is that they are only sensitive to the shape and not to the value of $I(V_{bias})$, and $I(V_{bias})$ measurements can be easily compared, even if the current values are vastly different. This is seen in Fig. 16, where I_{dark} and I_{light} differ by three orders of magnitude, and the ILD s are quite similar.

The breakdown voltage V_{bd} for the different methods is determined as the voltage at which

1. LD has its maximum.
2. The parabola through the 3 points around the minimum of ILD has its minimum.
3. The extrapolation of a straight-line (or parabola) fit of ILD for $V_{bias} > V_{bd}$ is zero.
4. The extrapolation of a straight-line fit of ILD for $V_{bias} < V_{bd}$ is zero
5. The second derivative of $\ln I(V_{bias})$ with respect to V_{bias} has its maximum.
6. A second order polynomial, fitted to $I(V_{bias})$ above V_{bd} after surface-current subtraction, crosses the V_{bias} axis.

Fig. 16 and Table 3 show the results of methods 1 – 4 for the KETEK SiPM PM15. Shown in the figure are I_{dark} and I_{light} with the scale on the right, and the corresponding $ILD(V_{bias})$ results with straight-line fits below and above V_{bd} , with the scale on the left. It is found that the results for V_{bd} from I_{dark} and I_{light} for $V_{bias} > V_{bd}$ agree within $\pm 20\text{ mV}$. The values found from

Method	1	2	3	4
V_{bd} from I_{dark} [V]	27.6	27.57	27.42	27.44
V_{bd} from I_{light} [V]	27.5	27.51	27.49	27.41

Table 3: Results of the different methods for determining V_{bd} for the KETEK SiPM with 15 μm pitch.

I_{dark} for methods 1 and 2 are systematically higher by ≈ 100 mV, which is related to the nearly constant I_{dark} for $V_{bias} < V_{bd}$, which results in a very high ILD value and shifts the ILD minimum to somewhat higher values.

In Ref. [19] method 5 is compared to methods 1 and 2, and agreement at the 100 mV is reported. To the knowledge of the author, a comparison at the 20 mV level is not available. In addition it is noted, that obtaining reliably second derivatives from experimental data can be quite tricky.

As discussed below, the second order polynomial of method 6, which is proposed in Ref. [10] and also recommended in Ref. [19], describes only the I_{dark} but not the I_{light} data for the KETEK SiPMs. Therefore it was not used. The method assumes the functional form for the Geiger breakdown probability $P_T \propto [1 - \exp(-\alpha \cdot (V_{bias} - V_{bd}))]$ for both I_{dark} and I_{light} . Apparently the functional form of $P_T(V_{bias})$ depends on the SiPM design and is also position dependent. As a result, a power-law fit $I(V_{bias}) \propto (V_{bias} - V_{bd})^n$ with the free parameter n , which is equivalent to method 3, is the safer approach.

For a quick and reliable determination at the 50 mV level it is recommended to use method 2 with the SiPM illuminated with DC light. In particular at low temperatures I_{dark} is so low that the measurement errors are significant, which makes the V_{bd} results unreliable. An idea about the dominant systematic uncertainties and a more precise determination can be obtained by varying the fit range in method 3 and by using a second order polynomial to fit ILD .

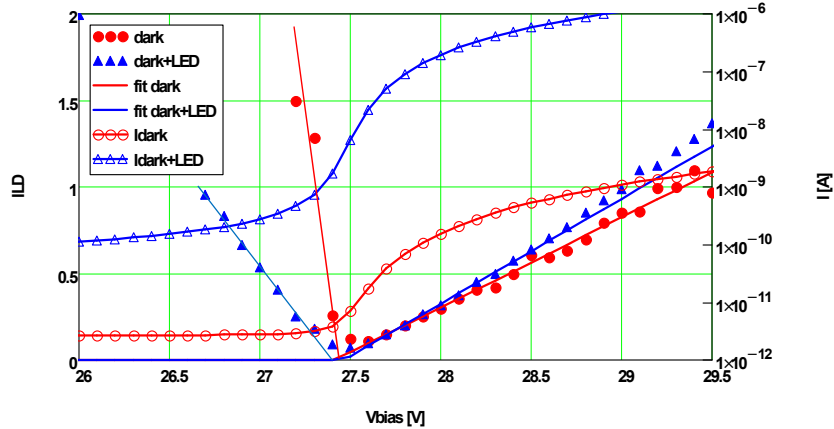


Figure 16: For the KETEK SiPM with 15 μm pitch measured at $+20^\circ\text{C}$: I_{dark} and I_{light} ($I_{dark+LED}$ in the figure) with the scale on the right, and the corresponding ILD values with straight-line fits below and above V_{bd} with the scale on the left.

From the fit using method 3 the inverse slope $1/n$ of ILD is obtained: n_{dark} from I_{dark} , and n_{photo} from I_{photo} . The values found for n_{dark} and for n_{photo} are 1.96 and 1.43, respectively. For an $I(V) = (V - V_{bd})^n$ dependence, $ILD(V_{bias}) = (V_{bias} - V_{bd})/n$. Thus a straight line of ILD means that above V_{bd} the current obeys the power law $I(V_{bias}) \propto (V_{bias} - V_{bd})^n$.

From n_{dark} and n_{photo} information on the position- and V_{bias} -dependence of the Geiger-discharge probability, P_T , can be obtained: Assuming a uniform, voltage-independent thermal volume-generation rate U_{gen} in the depletion region, i.e. ignoring high-field effects, the primary dark count rate $DCR_p = U_{gen} \cdot \langle P_T \rangle_{dep}$, and $I_{dark} = q_0 \cdot G \cdot DCR \cdot ECF \propto G \cdot \langle P_T \rangle_{dep} \cdot ECF$, where P_T is averaged over the entire depletion region. In the approximation $V_{bd} \approx V_{off}$, $G \propto (V_{bias} - V_{bd})^1$, and taking into account that $ECF \approx 1$ for small $V_{bias} - V_{bd}$ values, $\langle P_T \rangle_{dep} \propto$

$(V_{bias} - V_{bd})^{n_{dark}-1}$. The corresponding relation for the photo-current is: $I_{photo} = q_0 \cdot G \cdot N_\gamma \cdot PDE \cdot ECF \propto G \cdot \langle P_T \rangle_{photo} \cdot ECF$, from which follows $\langle P_T \rangle_{light} \propto (V_{bias} - V_{bd})^{n_{light}-1}$. Here the average of P_T is taken over the region in which the photons are absorbed, which extends only to $\approx 0.1 \mu\text{m}$ from the entrance window for the blue light used. Thus $n_{photo} - 1$ is related to $P_T(V_{bias})$ at the SiPM entrance window, and $n_{dark} - 1$ to $P_T(V_{bias})$ in the entire depletion region. This information can be used to validate simulations of the position dependence of P_T for different V_{bias} values.

Another approach of determining V_{bd} is presented in Refs. [19, 39]. The measured voltage dependence of PDE is fitted by the phenomenological function

$$PDE(V_{bias}) = PDE_{max} (1 - e^{-\mathfrak{D} \cdot V_{rel}}) \quad \text{with} \quad V_{rel} = \frac{V_{bias} - V_{bd}}{V_{bd}}, \quad (14)$$

with the phenomenological parameter \mathfrak{D} . The measurement of the PDE will be described in Sect. 4.4. The values found for V_{bd} agree with the values found using the methods described above, however the uncertainty is significantly larger. The authors point out that in first approximation \mathfrak{D} does not depend on the width of the multiplication region and conclude that the wavelength dependence $\mathfrak{D}(\lambda)$ reflects the position dependence of P_T . These results still have to be compared to simulations using the formulae given in Ref. [6] with realistic electric fields, or TCAD or Monte Carlo programs. In Ref. [7] a similar approach is followed: $PDE(V_{bias})$ is fitted with the dependence derived assuming that all electron-hole pairs are generated at the SiPM entrance window and a constant electric field in the depletion region of effective width w_{eff} . The values found for V_{bd} are again compatible with the values using the $I(V_{bias})$ methods.

The turn-off voltage, V_{off} , is obtained from the voltage dependence of the SiPM gain, $G(V_{bias}) \approx (C_d + C_q) \cdot (V_{bias} - V_{off})$, by fitting a straight line to the data and extrapolating to $G(V_{off}) = 1$. Examples for $G(V_{bias})$ for the KETEK SiPM with pitch values between $15 \mu\text{m}$ and $100 \mu\text{m}$ and the corresponding straight-line fits are shown in Fig. 17a. The determination of G and of the fluctuations of V_{off} is discussed in Sect. 4.4.

In Fig. 17b the differences $V_{bd} - V_{off}$ for the different pitch values of the KETEK SiPMs are shown. The V_{bd} value from $I(V_{bias})$ is labeled VI, and the one from PDE , VPD. The symbol used for V_{off} from $G(V_{bias})$ is labeled VG. The values found from VI and VPD are compatible, confirming that they both determine V_{bd} . However they differ from the values from VG, which determines V_{off} . The difference is approximately 1 V for the SiPM with $15 \mu\text{m}$ pixels and decreases with increasing pixel size. The reason for this dependence is not understood, however to the author's knowledge no simulations with realistic 3-D electric fields have been performed so far.

For the determination of V_{off} , instead of G derived from charge spectra, G from the pulse amplitude can also be used. The results obtained are compatible. Given the sensitivity of the amplitude to the band-width of the readout, in particular in the presence of a fast component, this method is not recommended.

In summary: A difference of up to 1 V between V_{bd} and V_{off} has been observed for a KETEK SiPM with a pitch of $15 \mu\text{m}$. For larger pitch values, the difference decreases. For the gain the relevant voltage is V_{off} , i. e. $G \propto (V_{bias} - V_{off})$. To avoid confusion, in publications it should be clearly stated, which voltage, V_{bd} or V_{off} , is used.

4.4. Photon-detection efficiency, number of primary Geiger discharges and gain

If peaks corresponding to different numbers of Geiger discharges, N_G , can be separated in the charge or amplitude spectra, the V_{bias} dependence of the relative PDE can be obtained from $f_{0,light}$ and from $f_{0,dark}$ using Eq. 7. Fig 18, taken from Ref. [19], shows the V_{bias} dependence of PDE for a number of wavelengths for two SiPMs. The relative values are obtained with the method described above.

The determination of the absolute PDE uses calibrated photo-diodes, as already discussed in Sect. 3.4. There are several setups, both at producers and at research laboratories, which measure the absolute PDE of SiPMs as function of wavelength and V_{bias} with an accuracy of a few %. Examples from Ref. [19] of the V_{bias} dependence of the absolute PDE are shown in Fig. 18, and

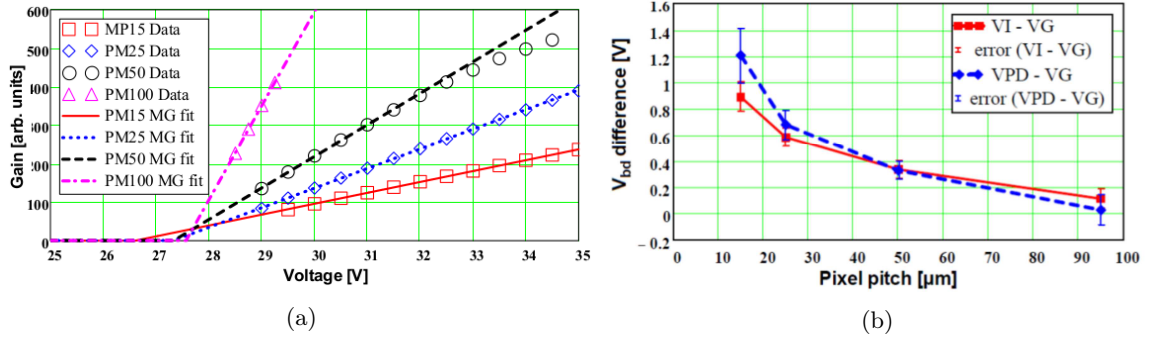


Figure 17: Results for the determination of V_{bd} and V_{off} for four KETEK SiPMs with different pitch from Ref. [7]. (a) Gain versus bias voltage, $G(V_{bias})$, and straight-line fits to determine the turn-off voltage V_{off} . (b) Difference $V_{bd} - V_{off}$ as a function of the pixel pitch. V_{off} from the $G(V_{bias})$ measurement is denoted VG, V_{bd} from $I(V_{bias})$ VI, and V_{bd} from $PDE(V_{bias})$ VPD.

of the wavelength dependence at a Geiger-breakdown probability $P_T \approx 90\%$, in Fig. 19. The accuracy achieved in these measurements is impressive, and so is the increase in PDE achieved by the producers in recent years.

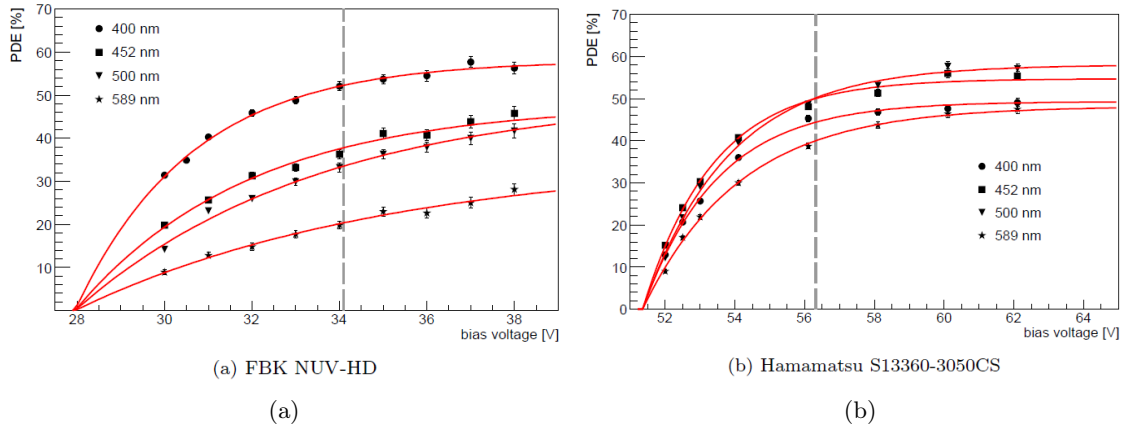


Figure 18: Photon-detection efficiencies $PDE(V_{bias}, \lambda)$ as a function of V_{bias} and the wavelength λ of the light, for two SiPMs from Ref. [19]. The vertical lines denote the bias voltage at which 90% of the maximum PDE is reached. The pixel pitch is $30\mu\text{m}$ for the FBK SiPM, and $50\mu\text{m}$ for the Hamamatsu SiPM. In addition, the design of the two SiPMs is different and optimised for different wavelengths, which has to be taken into account when judging the PDE dependencies.

Next, different methods of determining the SiPM gain are discussed. The most straight-forward method of measuring the gain, $G^*(V_{bias})$, of the combined system SiPM-readout, is to record charge spectra, as shown in Fig. 3, and determine the distance between the peaks corresponding to different number of Geiger discharges. Several methods are used:

1. Fit individual peaks by Gauss functions and determine the distance between them.
2. Determine the distance using the Fourier transformed spectrum (Ref. [23]).
3. Perform a complete fit of the spectrum with G^* as one of the free parameter of the fit (Ref. [11]).

All three methods give very precise and compatible results, and it is matter of taste and convenience which one to use. However, they all require that 0, 1, 2, etc. are well separated.

In addition to G , the rms width σ_{N_G} of the peaks corresponding to different number of Geiger discharges, N_G , can be obtained from the spectra. As expected and observed, the data can be described by $\sigma_{N_G}^2(V_{bias}) = \sigma_0^2 + N_G \cdot \sigma_1^2(V_{bias})$, with σ_0 the contribution from the electronics

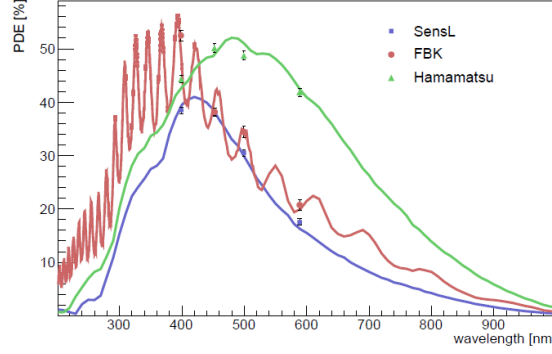


Figure 19: PDE as a function of wavelength between 200 nm and 1000 nm for three SiPMs from Ref. [19]. V_{bias} has been adjusted to give a Geiger-breakdown probability $P_T \approx 90\%$.

noise and $\sigma_1(V_{bias})$ the contribution from the fluctuations of G for single Geiger discharges. For the KETEK SiPM investigated in Ref. [11] it is found that σ_1 has only a weak V_{bias} dependence: Between $V_{bias} = 30$ V and 35 V it increases by $\approx 20\%$ only. For this SiPM $V_{bd} = 26.64$ V at 20°C . As $G = (C_d + C_q) \cdot (V_{bias} - V_{off})$, there are two contributions to σ_1 . One from the pixel-to-pixel variations of $C_d + C_q$, called δC , and one from the fluctuations of V_{off} , called δV_{off} . The two terms can be distinguished using the V_{bias} dependence of σ_1 . Using the measured slope dG/dV_{bias} and the definition of G , one finds:

$$\sigma_1^2 = \left(\frac{dG}{dV_{bias}} \right)^2 \cdot \delta V_{off}^2 + \left(\frac{dG}{d(C_d + C_q)} \right)^2 \cdot \delta C^2 = (C_d + C_q)^2 \cdot \delta V_{off}^2 + (V_{bias} - V_{off})^2 \cdot \delta C^2. \quad (15)$$

As σ_1 is approximately independent of V_{bias} , the second term is small and: $\delta V_{off} \approx \sigma_1 / (C_d + C_q)$, giving $\delta V_{off} \approx 175$ mV for the data from Ref. [11]. It is concluded that the increase of the width of the peaks in the SiPM charge (or amplitude) spectra is caused by differences in V_{off} and not by differences in pixel capacitances. The reason for the rather large value of δV_{off} could be differences of the 3-D electric field distribution within a pixel. To the author's knowledge, no realistic simulations of V_{off} and δV_{off} have been performed so far.

If $N_G = 0, 1, 2, \dots$ peaks can not be separated, the gain, G^* , and the mean number of primary Geiger discharges, $\langle N_{pG} \rangle$, can nevertheless be determined from the mean, $\langle Q \rangle$, and the root-mean square, σ_Q , of the measured charge (or amplitude) distribution if the excess charge factor, ECF , and the excess noise factor, ENF , are known. The method is an extension of the well known method used to determine the gain, G^* , and the mean number of photo-electrons, $\langle N_{pe} \rangle$, for vacuum photomultipliers, which are (incorrectly) assumed to be ideal photon-detectors with $ECF = ENF = 1$. For the ideal photomultiplier the distribution of the photo-electrons generated by the pulsed light is assumed to follow a Poisson distribution, for which both mean and variance are equal to $\langle N_{pe} \rangle$. With the gain G^* , the mean of the measured charge distribution becomes $\langle Q_P \rangle = q_0 \cdot G^* \cdot \langle N_{pe} \rangle$, and the square of the rms spread $\sigma_P^2 = q_0^2 \cdot G^{*2} \cdot \langle N_{pe} \rangle$. The subscript P , which stands for *Poisson*, refers to the ideal detector. From these two equations follows:

$$G^* = \frac{\sigma_P^2}{q_0 \cdot \langle Q_P \rangle} \quad \text{and} \quad \langle N_{pe} \rangle = \frac{\langle Q_P \rangle^2}{\sigma_P^2}. \quad (16)$$

For a non-ideal SiPM, ECF and ENF , defined in Eq. 4 and 5, have to be taken into account, which results in

$$\langle Q \rangle = ECF \cdot \langle Q_P \rangle = ECF \cdot q_0 \cdot G^* \cdot \langle N_{pG} \rangle, \quad \text{and} \quad (17)$$

$$\sigma_Q^2 = ECF^2 \cdot ENF \cdot \langle Q_P \rangle = ECF^2 \cdot ENF \cdot q_0^2 \cdot G^{*2} \cdot \langle N_{pG} \rangle, \quad (18)$$

where for the SiPM the mean number of photo-electrons of the vacuum photomultiplier, $\langle N_{pe} \rangle$, has been replaced by the mean number of primary Geiger discharges $\langle N_{pG} \rangle$. Solving the two

equations for G^* and $\langle N_{pG} \rangle$ gives

$$G^* = \frac{\sigma_Q^2}{q_0 \cdot \langle Q \rangle \cdot ECF \cdot ENC} \quad \text{and} \quad \langle N_{pG} \rangle = \frac{\langle Q \rangle^2 \cdot ENF}{\sigma_Q^2}. \quad (19)$$

A method to determine ECF and ENC is presented in Sect. 4.5.

In Ref. [11] the results for $\langle N_{pG} \rangle$ and G^* determined by a fit to the charge distribution are compared to the ones from $\langle Q \rangle$ and σ_Q for the KETEK SiPM with 15 μm pitch illuminated with a pulsed LED. Fig. 20 shows the results. For both $\langle N_{pG} \rangle$ and G^* the agreement is within a few percent, demonstrating the validity of the method. This method is straight-forward to use and suitable for the in-situ calibration and the monitoring of large numbers of SiPMs. It is used routinely in Ref. [40]. It should be noted that in the case of significant noise, the width of the $N_G = 0$ peak has to be subtracted quadratically from σ_Q . In addition, it should be mentioned that the method as described does not work if the response of the system SiPM–readout is non-linear. But it is straight-forward to extend the method to non-linear regions, which, however, to the author’s knowledge, has not yet been reported.

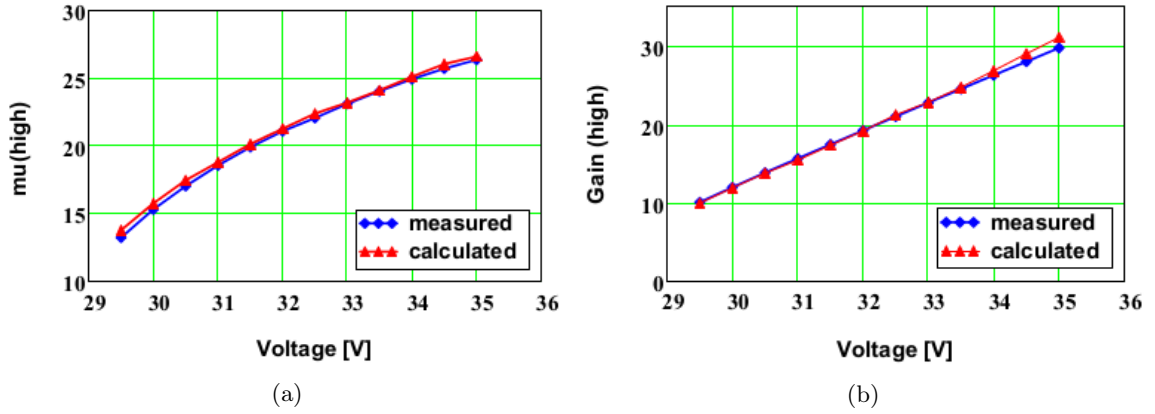


Figure 20: Comparison of (a) the average number of primary Geiger discharges, $\mu \equiv \langle N_{pG} \rangle$, and (b) the gain G^* from a fit to the measured charge spectrum (measured) with the method of the moments of the charge distribution (calculated) using Eq. 19. The figure is from Ref. [11], which also gives the corresponding values of ECF and ENF .

4.5. Nuisance parameters: Dark-count rate and correlated noise

Compared to an ideal photon-detector, the SiPM performance is affected by a number of nuisance sources, in particular random dark counts and pulses correlated with primary discharges. The different types of nuisance parameters have been discussed in Sect. 2. The best way to study them in detail, is to record current transients without or with low-intensity illumination. The analysis and results presented in Ref. [19] will be discussed next. The analysis procedure used follows closely the one reported in Ref. [13]. Similar analyses are reported in Refs. [41, 42, 43].

In Ref. [19] the transients are differentiated by subtracting a copy of the transient shifted by 3 ns (see Fig. 21a). In this way the pulse tails are removed and the pulses have a full width of about 9 ns. Next the undershoot is removed by applying a background-subtraction algorithm, and pulses with an amplitude exceeding 0.5 pe (pe = the average amplitude of a single Geiger discharge) are marked. Finally pulses corresponding to single Geiger discharges are selected, and the time difference Δt to the following pulse versus its amplitude plotted, as shown in Fig. 21b. Note that the Δt scale and the Δt bin widths are logarithmic.

Dark counts without correlated noise have an average amplitude corresponding to one Geiger discharge. They appear as horizontal line around $\text{pe} = 1$. Dark-count pulses with one or two prompt optical cross-talk pulses, each with an amplitude of 1 pe, appear as horizontal lines at $\text{pe} = 2$ and 3, respectively. After-pulses have an amplitude which increases with time due to the recharging of the pixel (see also Fig. 4b). Pulses with delayed optical cross-talk are the sum

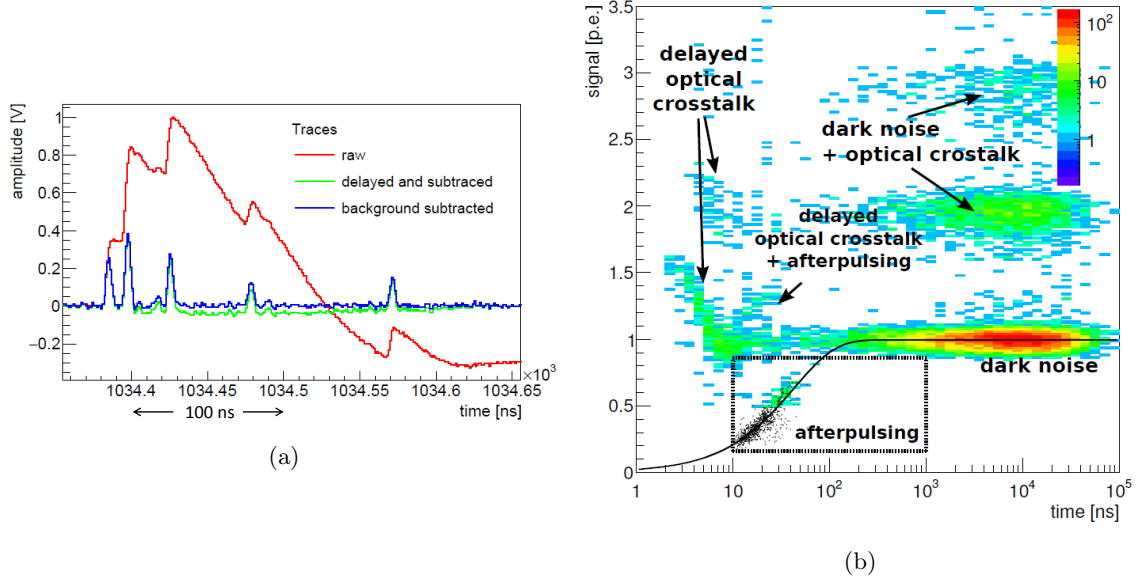


Figure 21: Analysis and results for the determination of the nuisance parameters using current transient measurements from Ref. [19]. (a) A SiPM transient recorded with 1 GS/s and 8 bit resolution (raw), after subtraction of the transient shifted by 3 ns (delayed and subtracted), and after the undershoot correction (background subtracted). (b) 2-D plot of the number of events in bins of the logarithm of the time difference between two consecutive SiPM pulses (x axis) and the amplitude of the second pulse (y axis), after selecting pulses corresponding to single Geiger discharges (1 pe) for the first pulse. As explained in the text and indicated on the figure, dark counts and the different types of correlated noise events can be classified and identified.

of the decaying pulse of the primary Geiger discharge and one or two optical cross-talk pulses, each with an amplitude of 1 pe. Their amplitudes decrease towards $\text{pe} = 1$ or 2 with increasing Δt . By selecting events in the different regions, all nuisance parameters can be determined in a quantitative way. In the following a few examples are given.

The total dark-count rate, DCR , can be approximately determined by counting all pulses and dividing the number by the total duration of all analysed transients. DCR is given by the primary dark count rate plus the effects of after-pulses and delayed optical cross-talk. A more precise procedure is to analyse the Δt distribution, $dN/d\Delta t$, which for random dark pulses at the rate DCR is expected to have the form $dN/d(\Delta t) \propto e^{-(\Delta t \cdot DCR)}$. This dependence follows from the properties of the Poisson distribution: The mean number of dark counts (DC) in the time interval Δt is $\langle N(\Delta t) \rangle = DCR \cdot \Delta t$, and the probability of zero DC s in Δt is $P(0, \Delta t) = e^{-(\Delta t \cdot DCR)}$. The absolute value of the derivative $|dP(0, \Delta t)/d(\Delta t)| = DCR \cdot e^{-(\Delta t \cdot DCR)}$ is proportional to the probability of the change from 0 to ≥ 1 DC s, thus the occurrence of a DC at Δt . The Δt distribution for random dark counts, when plotted in bins of $\ln(\Delta t)$, is $\propto \Delta t \cdot e^{-(\Delta t \cdot DCR)}$ with the maximum at $\Delta t_{max} = 1/DCR$. This can be clearly seen in Fig. 21b.

Fig. 22a shows an example of a $dN/d(\ln(\Delta t))$ distribution with a fit of the expected DC dependence for $\Delta t > 200$ ns. At lower Δt values the effects of correlated pulses are clearly visible. In Refs. [21, 30] the Δt distribution in linear Δt scale is fitted to the sum of DC s and after-pulses with exponential time distributions. If only DC s and after-pulses are considered, the expected Δt distribution can be derived by replacing $\langle N(\Delta t) \rangle = DCR \cdot \Delta t$ valid in the absence of after-pulses and delayed cross-talk, by $\langle N(\Delta t) \rangle = DCR \cdot \Delta t + \varepsilon_{AP} \cdot (1 - e^{-\Delta t/\tau_{AP}})$ for one state, with the probability of after-pulses, ε_{AP} , and the time constant τ_{AP} . Differentiation of $P(0, \Delta t) = e^{-\langle N(\Delta t) \rangle}$ with respect to Δt gives the Δt dependence. Fig. 22b shows an example of such an analysis from Ref. [30], which shows that the data are well described by the model and that DCR , ε_{AP} and τ_{AP} are determined with good accuracy. Delayed cross-talk can be implemented in a similar way, if a parametrisation for its time dependence is available.

The DCR can also be obtained from charge or amplitude spectra measured without illumina-

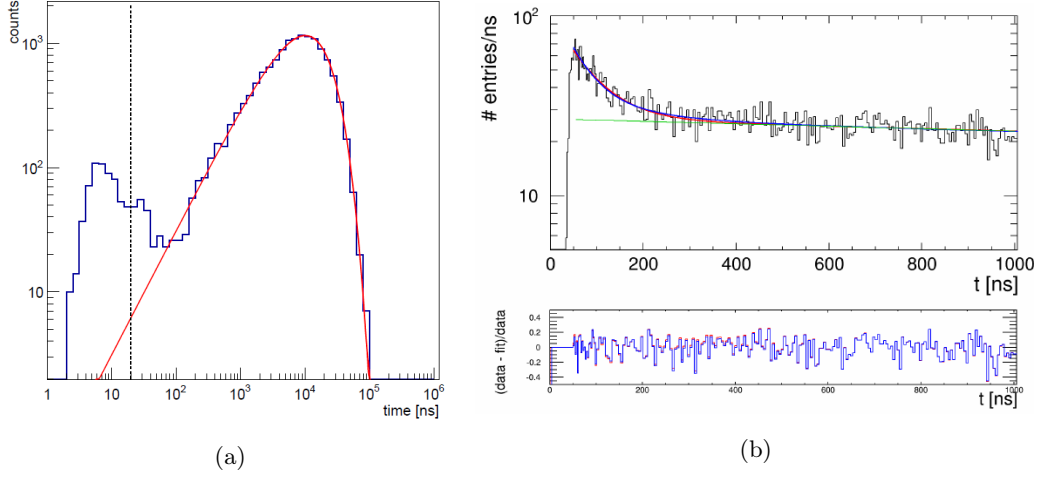


Figure 22: (a) Time difference Δt in logarithmic Δt scale from Ref. [19]. The solid line is a fit for $\Delta t > 200$ ns by $\Delta t \cdot e^{-(\Delta t \cdot DCR)}$, the expected shape for random dark-count pulses in $\log(\Delta t)$ bins. The maximum of the peak is at $1/DCR$. (b) Top: Time-difference distribution in linear Δt scale for a Hamamatsu SiPM from Ref. [30]. The solid lines are fits of the sum of dark counts and after-pulses for $\Delta t > 50$ ns, where the algorithm for the identification of after-pulses is fully efficient. The essentially straight line is the contribution of dark counts. Bottom: Difference $(\text{data} - \text{fit}) / \text{data}$.

tion, as the one shown in Fig. 3a, using the relation

$$DCR = -\frac{\ln(f_{0.5, \text{dark}})}{t_{\text{gate}}}, \quad (20)$$

with $f_{0.5, \text{dark}}$, the fraction of events with a charge exceeding half the signal of a single Geiger discharge ($1/2$ pe), and t_{gate} the gate width used for the current integration. As gate and dark pulses are uncorrelated in time, the charge spectrum contains pulses with different overlaps with the gate, resulting in signals between the $N_G = 0$ and the $N_G = 1$ peak. In Ref. [11] it is shown, that only for $f_{0.5, \text{dark}}$ Eq. 20 is exact. If a lower or a higher threshold than 0.5 pe is chosen, the value for t_{gate} in Eq. 20 has to be decreased or increased with respect to the actual t_{gate} . Thus fitting the $N_G = 0$ peak and using the fraction of events in the peak instead of $f_{0.5, \text{dark}}$, which is frequently done, is only approximate and should be avoided. In cases where the tail of the zero-Geiger discharge peak results in a significant fraction of events above 0.5 pe, these events have to be subtracted when determining $f_{0.5, \text{dark}}$. It should be noted that after-pulses and delayed cross-talk result in a systematic bias of this DCR determination. It is estimated that the effect is small, but a systematic study is not known to the author.

To summarise: The $f_{0.5, \text{dark}}$ method is straight-forward and recommended for determining the DCR , but has a bias, which however in most practical cases will be small. For a more precise determination, the Δt method described above should be used.

The methods described so far can only be applied if peaks corresponding to different number of Geiger discharges can be distinguished. Determining DCR when this is not the case, is significantly more complex and a number of assumptions have to be made in the analysis. Fig. 23, which shows current transients with low light for a SiPM before irradiation (a), and after irradiation (b), shows the problem. Whereas in (a) it is straight-forward to analyse the single Geiger discharge pulse, this is impossible for (b), which shows wild fluctuations with amplitudes, which are larger by one order of magnitude. Transients, as shown in Fig. 23b, can be reproduced by a simple Monte Carlo simulation by adding $DCR \cdot \Delta t_{\text{trans}}$ pulses as shown in Fig. 23a randomly distributed in the time interval of the transient, Δt_{trans} . For estimating DCR in such a situation, two methods will be described. One uses the measured dark current, I_{dark} , the other σ_{dark} , the *rms* of the charge distribution measured without illumination. These methods are discussed in Ref. [44] and used in Ref. [15] to characterise radiation-damaged SiPMs. At high DCR values, I_{dark} can exceed several

mA and an AC-coupled readout is typically used, so that the average current is zero and contains no information. In addition, the high current results in a significant power dissipation causing an uncertainty in the knowledge of the SiPM temperature.

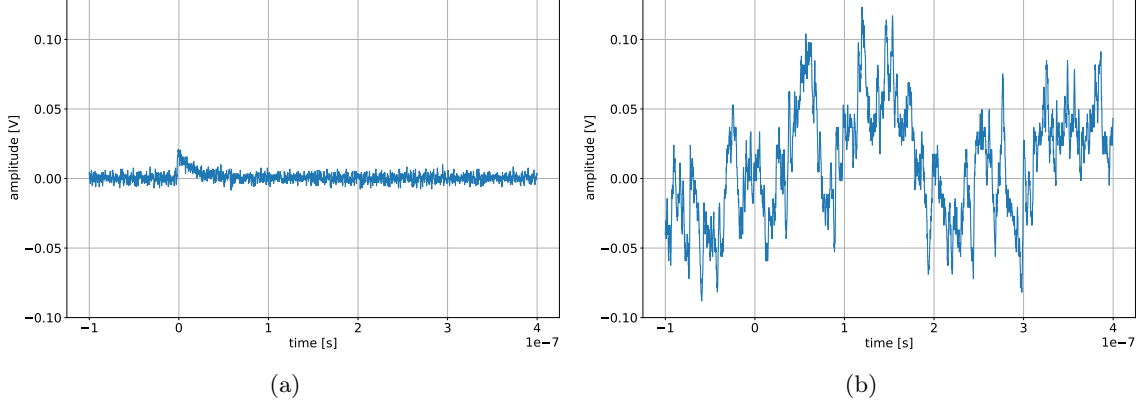


Figure 23: Transients recorded with a KETEK PM15 SiPM at 29.4 V and -30°C for (a) before irradiation, and (b) after irradiation by neutrons to a fluence of $5 \times 10^{13} \text{ cm}^{-2}$ causing a $DCR \approx 3 \text{ GHz}$.

I_{dark} is related to the primary dark count rate DCR_p by

$$I_{dark} = q_0 \cdot G \cdot ECF \cdot DCR_p = q_0 \cdot (C_d + C_q) \cdot (V_{bias} - V_{off}) \cdot ECF \cdot DCR_p, \quad (21)$$

from which follows

$$DCR_p(V_{bias}) = \frac{I_{dark}}{ECF(V_{bias}) \cdot q_0 \cdot (C_d + C_q) \cdot (V_{bias} - V_{off})}. \quad (22)$$

C_d and C_q can be determined from $Y-f$ (Sect. 4.1), and V_{bd} from $I-V$ measurements (Sect. 4.3). If the approximation $V_{off} \approx V_{bd}$ is made, which is valid for $V_{OV} \gg V_{bd} - V_{off}$, $ECF \cdot DCR_p$ can be obtained using Eq. 22. As ECF is typically $\lesssim 1.2$, $ECF \cdot DCR_p$ is already a quite good approximation to DCR . An alternative, which is used in Refs. [15, 44] for the study of radiation damage, is to assume that ECF and $V_{bd} - V_{off}$ do not change with irradiation, and determine V_{bd} from the $I-V$ measurements. The validity and accuracy of these assumptions has not been checked so far.

Next, the determination of DCR_p from the measurement of the rms-spread, σ_{dark} , of the charge (or amplitude) distribution measured without illumination, will be discussed. Fig. 24a shows charge spectra measured with a gate width $t_{gate} = 75 \text{ ns}$ without illumination for the KETEK PM15 SiPM irradiated by neutrons to different fluences up to $5 \times 10^{14} \text{ cm}^{-2}$. As discussed in detail in Ref. [15], the dominant effect of radiation damage is the increase of DCR by many orders of magnitude. One sees that σ_{dark} first increases with fluence, and above a fluence of $5 \times 10^{13} \text{ cm}^{-2}$ decreases. For high DCR values many pixels are already busy with Geiger discharges, and this high occupancy is responsible for the decrease of σ_{dark} . The formula used to extract DCR_p from σ_{dark} is:

$$\sigma_{dark}^2 = ((q_0 \cdot G)^2 \cdot ENF \cdot ECF^2 \cdot DCR_p) \cdot (t_{gate} - \tau_r \cdot (1 - e^{-t_{gate}/\tau_r})). \quad (23)$$

It is derived in the appendix, under the assumption that the SiPM current pulse for a Geiger discharge at time t_0 is described by $I(t) \propto e^{-(t-t_0)/\tau_r}$ for $t \geq t_0$. An extension to other pulse shapes is straight-forward inserting the functional form of $f(t)$ in Eq. 27. To verify the predicted t_{gate} dependence, Fig. 24b compares the measured $\sigma_{dark}^2(t_{gate})$ (symbols) to fits by Eq. 23 (solid lines) with τ_r and the term in the parenthesis on the left side, as free parameters. The dependence of ECF and ENF on t_{gate} has been neglected in the fits. Up to a fluence of 10^{13} cm^{-2} the data are well described, and allow to determine τ_r with an accuracy of about 10 %. For fluences exceeding

10^{13} cm^{-2} , the quality of the fit worsens because of the high pixel occupancy at high DCR . For low DCR , σ_{dark} is dominated by electronics noise, which has to be subtracted quadratically from σ_{dark} . If the electronics noise dominates, the method becomes unreliable. A formula, which takes into account the reduction of σ_{dark} due to pixels occupied by dark counts, still has to be derived. In order to determine DCR_p from Eq. 23, assumptions for G , ECF and ECN have to be made. For the determination of G^* , when peaks corresponding to different Geiger discharges cannot be distinguished, Eq. 19 can be used. For the determination of ECF and ENF no method is known to the author, if peaks corresponding to different number of Geiger discharges can not be distinguished. However, in most practical cases the problem of merging peaks is either the result of ambient light or of radiation damage. In these cases, ECF and ENF can be measured initially, and the assumption made that the values do not change for the conditions in which the SiPM is finally used. The validity of these assumptions for radiation damage still has to be demonstrated.

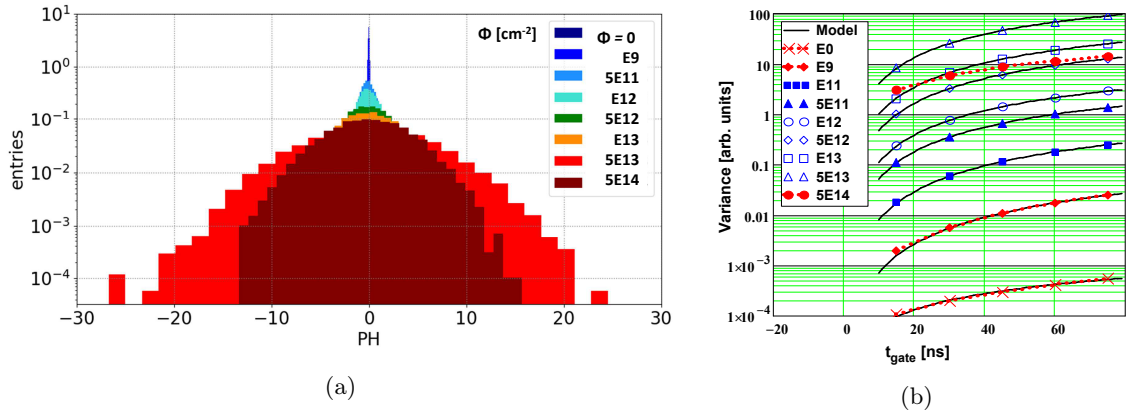


Figure 24: (Colour online) (a) Charge spectra measured at -30°C in the dark for KETEK MP15 SiPMs after irradiation to different neutron fluences, Φ . Measurements and figure are from S. Cerioli, Hamburg University. (b) Variances, σ_{dark}^2 , of the charge spectra as a function of the gate width, t_{gate} . The symbols are the data, and the lines the fits by Eq. 23 with τ_r and the term in the left parenthesis of Eq. 23 as free parameters. Solid lines represent good, and dotted lines poor description of the data by the fit.

In Ref. [15], DCR_p is determined as a function of the neutron fluence using the measured I_{dark} and Eq. 23, assuming for ECF and ENF the values of the non-irradiated SiPM. The results are compared to the DCR_p results using Eq. 22, assuming ECF and $V_{bd} - V_{off}$ from the non-irradiated SiPM and the values of V_{bd} from the $I - V$ analyses for the different neutron fluences. In the range of the validity of the σ_{dark} method an agreement to better than 30% is observed, which is considered satisfactory for DCR values exceeding several GHz. A detailed comparison of the methods and their sensitivity to the assumptions used is still missing.

To summarise this subsection on the DCR and DCR_p determination: If the DCR is sufficiently low and the peaks for different number of Geiger discharges can be distinguished, the different methods, counting the dark-counts in the transients, analysing the time-difference Δt , and the $f_{0.5, dark}$ method, are straight-forward and give reliable results. For DCR values approaching or exceeding $1/\tau_r$, the pixel-recharging time constant (typically between 15 and 200 ns), the situation becomes significantly more complicated. Based on ongoing studies, the preliminary conclusion is that for high DCR s using I_{dark} and Eq. 22 is the most reliable method to determine DCR_p . This method however, requires the knowledge of G and ECF . For G it is recommended to use $G = (C_q + C_d) \cdot (V_{bias} - V_{off})$, with $C_d + C_q$ from $Y - f$ (admittance-frequency) measurements for V_{bias} 0.5 to 1 V below V_{bd} . For V_{off} , V_{bd} can be used, which however is a poor assumption for small V_{OV} values if V_{bd} differs significantly from V_{off} . If the difference $V_{bd} - V_{off}$ can be determined for a low DCR , then the assumption of a constant difference can be made, and V_{bd} obtained from $I_{dark} - V_{bias}$ measurements. To better understand the effects of high DCR , the following study is recommended: For a SiPM, with properties precisely determined using the methods of individual Geiger discharges, different DCR values can be simulated by DC-light of

variable intensity illuminating uniformly the SiPM. In this way the different methods can be compared and the most suitable determined.

Cross-talk, after-pulses, ECF, ENF and optimal resolution

Fig. 21b shows the 2-D distribution of the time between pulses, Δt , versus pulse amplitude, which allows identifying the different physical effects responsible for the nuisance parameters. Analysing separately the different event classes allows to study their rate and properties. These studies as a function of V_{bias} and temperature are essential for understanding the different effects and proposing technological modifications of the fabrication process to improve the SiPM performance. They also provide input for the development of realistic SiPM models. An example is given in Fig. 22 with the discussion on the extraction of after-pulses and delayed cross-talk.

However, as long as saturation effects can be ignored, for most users the knowledge of DCR , G^* , ECF and ENF as a function of V_{bias} of the SiPMs will be sufficient to characterise the SiPM and determine the optimal operating conditions. These parameters depend not only on the SiPM properties, but also on the readout used. As an example: A shorter integration of the SiPM current, results in a reduction of G^* , ECF and ENF .

The most direct way to determine these parameters uses two charge spectra: One recorded in the dark (Q_{dark}), and one with low-intensity light (Q), so that the fraction of events in the peak for zero Geiger discharges can be measured precisely. In the following it is assumed that the mean of the zero-Geiger discharge peak corresponds to zero charge. DCR is obtained using Eq. 20 from the Q_{dark} spectrum and G^* from the distance between the peaks of the Q spectrum, as discussed in Sect. 4.4. The mean number of primary Geiger discharges due to photons from the light source, $\langle N_{pG, photo} \rangle$, is obtained from Eq. 7. ECF is obtained from the ratio of the mean of the measured charge distribution $\langle Q \rangle$ to the expectation for a Poisson distribution $q_0 \cdot G^* \cdot \langle N_{pG, photo} \rangle$, and ENF from the ratio of the square of the rms-spread, σ_Q^2 , to the Poisson expectation $(q_0 \cdot G^*)^2 \cdot \langle N_{pG, photo} \rangle$:

$$ECF = \frac{\langle Q \rangle}{q_0 \cdot G^* \cdot \langle N_{pG, photo} \rangle} \quad \text{and} \quad ENF = \frac{\sigma_Q^2}{(q_0 \cdot G^*)^2 \cdot \langle N_{pG, photo} \rangle}. \quad (24)$$

The rms-spread σ_{dark} allows to estimate the contribution of dark counts to the ENF .

To illustrate the use of ENF , the calculation of the operating voltage at which the photon resolution is optimal is presented. Inserting $\langle N_{pG} \rangle$ from Eq. 3 into Eq. 17 and 18 one obtains for the relative resolution

$$\frac{\sigma_Q}{\langle Q \rangle} = \sqrt{\frac{ENF}{N_\gamma \cdot PDE}}. \quad (25)$$

Both ENF and PDE increase with V_{bias} . Whereas PDE eventually saturates, ENF continues to increase, and the relative resolution has a minimum. An example of such a dependence is given in Ref. [11]. As both ENF and G^* depend on the effective charge integration time, Eq. 25 can also be used to optimise the readout electronics.

4.6. Non-linearity and saturation

For calorimetric measurements, e.g. in collider and astro-physics experiments or in PET, the dynamic range, i.e. the range of N_γ , where precise measurements are possible, is an essential parameter. High gain, high PDE , single photon-detection and high dynamic range are conflicting requirements, which can hardly be achieved simultaneously. In this respect vacuum photomultipliers are superior to SiPMs. A major complication is that all the nuisance parameters discussed so far enter in one way or another into the dynamic range. In addition, the pulse shape is expected to depend on the number of simultaneous Geiger discharges, and because of the pixel recharging time constant, the dynamic range depends on the time distribution of the photons. In spite of the high relevance of the dynamic range, systematic studies so far are quite scarce.

In Ref. [45] light from a laser with a wavelength of 404 nm and a pulse-width of 32 ps has been used to investigate the dynamic range of simultaneously arriving photons, up to a photon

intensity at which $\approx 500 \times N_{pix}$ Geiger discharges would be triggered simultaneously, if the SiPM were linear. Four different SiPMs with 1 mm^2 area and $N_{pix} = 100, 400, 556$ and 560 from Hamamatsu, Photonique and Zecotek were investigated. Measured was the amplitude of the SiPM pulse recorded with a digital scope as a function of the relative number of photons, $N_{\gamma,rel}$, called N_{seed} in the paper. $N_{\gamma,rel}$ is proportional to the current in a PIN photo-diode with a linear response, normalised so that $N_{\gamma,rel} = \langle N_G \rangle$ for low light intensities, where the SiPMs are known to be linear. The measurements were performed for $V_{bias} - V_{bd}$ values between 0.5 V and 1.3 V . The way V_{bd} has been determined is not reported in the paper. Fig. 25 shows the results. It is observed that at high light intensities for all SiPMs the mean number of measured Geiger discharges, $\langle N_G \rangle$, significantly exceeds the number of pixels, N_{pix} , and $\langle N_G \rangle$ does not appear to reach a constant saturation value. Thus the expectation given in Eq. 6 is not observed. Various explanations of this phenomenon are discussed in the paper, but the conclusion is: *Up to now, no convincing explanation for this over saturation and enhanced dynamic range could be found.*

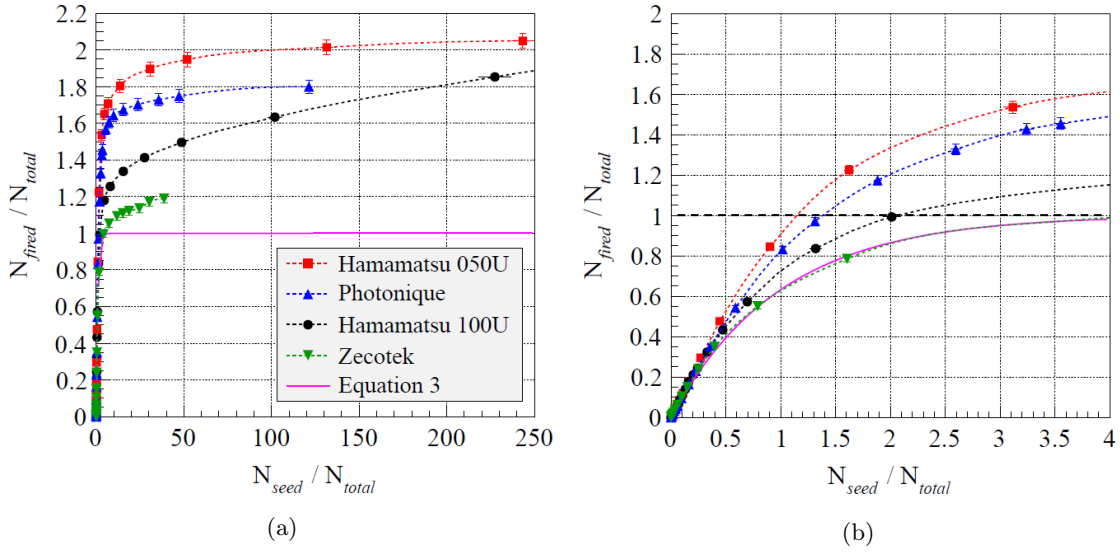


Figure 25: Dynamic range results using amplitude measurements from Ref. [45]. Shown is $\langle N_G / N_{pix} \rangle$ (in the figure N_{fired} / N_{total}) versus $N_{\gamma,rel} / N_{pix}$, the ratio of the expected number of Geiger discharges for a hypothetical linear SiPM without saturation to N_{pix} (in the figure N_{seed} / N_{total}) for (a) $\langle N_G \rangle / N_{pix} < 250$, and (b) expanded view with $\langle N_G \rangle / N_{pix} < 4$. In all cases a significant excess of the number of measured Geiger discharges above N_{pix} (lines for $N_G / N_{pix} = 1$) is observed.

Note, that it is expected that the pulse amplitude, which was used in the described measurements, depends on the number of Geiger discharges in a pixel. The reason is that n micro-plasma tubes in a pixel correspond to n resistors R_d in parallel in the electrical model shown in Fig. 1b, which results in a decrease of the time constant of the Geiger discharge and thus in a higher amplitude of the fast pulse. This effect has been reported in Ref. [46]. Whereas the charge was found to be independent of n , the current amplitude increased with n . It also should be noted, that the fast component of the pulse has a rise time of typically several tens of ps and a full width below 1 ns . Therefore the measured pulse amplitude is very much influenced by the bandwidth of the readout.

A study with a picosecond laser, however using charge- instead of amplitude-measurements, for four SiPMs from Hamamatsu ($N_{pix}/pitch [\mu\text{m}] = 2668/25, 1600/25, 400/50$ and $100/100$) has been presented by G. Weitzel [47] and S. Krause [48]. The results are shown in Fig. 26. $N_{total} (\equiv N_{pix})$ is the number of pixels, N_{seed} the number of Geiger discharges expected in the absence of saturation, and $N_{fired} (\equiv \langle N_G \rangle)$ the measured mean number of Geiger discharges. N_{seed} is obtained by scaling N_{γ} so that $N_{seed} = N_{fired}$ for low N_{γ} , where the SiPM response is known to be linear. The data were fitted by $\mu_c \cdot (1 - e^{-N_{seed}/(\mu_c \cdot N_{total})})$, where $\mu_c = N_{G,sat}/N_{pix}$, and $N_{G,sat}$ the saturation value of N_G for high light intensities. For the SiPMs with $50\text{ }\mu\text{m}$ and $100\text{ }\mu\text{m}$ pitch, the values

found for μ_c are significantly larger than 1 and similar to the findings of Ref. [45]. The SiPMs with 25 μm pitch shows μ_c values compatible with or closer to 1. An explanation for the difference could be the merging of micro-plasma channels from Geiger discharges in the same pixel for small pixels. Clearly, more studies are needed to understand these results.

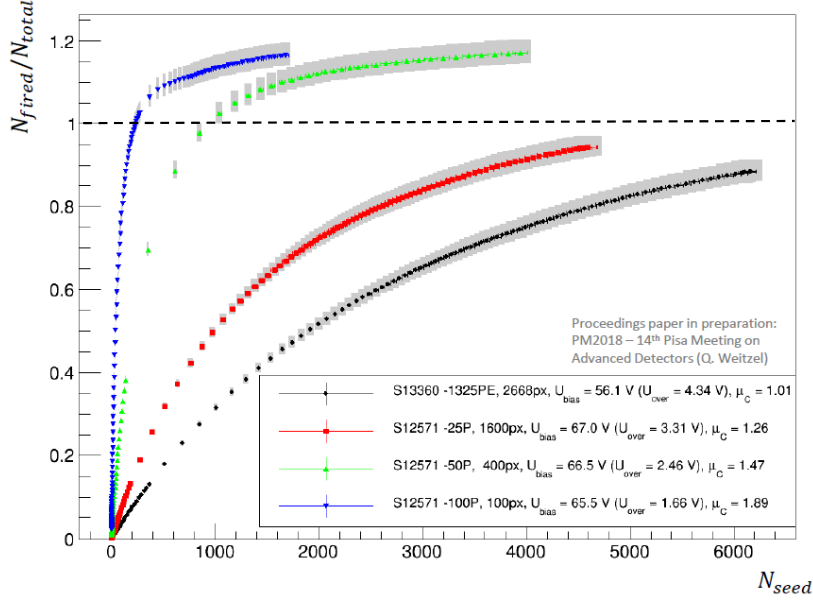


Figure 26: Dynamic-range measurements from Refs. [47, 48]. The same quantities as in Fig. 25 are shown, however the charge instead of the amplitude was measured for the four different Hamamatsu SiPMs. The insert gives bias voltage (U_{bias}), over-voltage (U_{over}), and μ_c , the ratio of the saturation value of $\langle N_G \rangle / N_{\text{pix}}$ from the fit.

In Ref. [14] the dynamic range for light pulses of different durations is studied. As light source a LED is used, driven by a computer controlled pulse generator to generate light pulses of up to $\tau_{\text{light}} = 100$ ns duration and photon numbers hitting the SiPM, N_γ , of up to $> 10^5$. The SiPMs investigated were fabricated by KETEK with $N_{\text{pix}} = 3600$ and $\text{pitch} = 50 \mu\text{m}$, and by Hamamatsu with $N_{\text{pix}} = 900$ and $\text{pitch} = 100 \mu\text{m}$. Fig. 27 shows the dependence of $\langle N_G \rangle$ after correction for dark pulses (called n_{eff}) on N_γ . The value of N_{pix} is shown as a dashed line. For the KETEK SiPM the charge was recorded with a 400 ns gate and for the Hamamatsu SiPM with a 150 ns gate. The authors conclude that in the linear range (which extends to $n_{\text{eff}} \approx 0.2 \cdot N_{\text{pix}}$), the response is independent of τ_{light} . For higher N_γ values the response increases with τ_{light} , as does the saturation value. The ratio of the saturation value to N_{pix} for the SiPM with 100 μm pixels is larger than for the one with 50 μm , which agrees with the observations of Refs. [47, 48].

To summarise: The dynamic range of SiPMs is determined by four factors: The number of pixels, N_{pix} , the pixel recharging time, τ_r , the correlated noise, and the pixel occupancy due to dark counts. As long as the number of photons generating simultaneously primary Geiger discharges and the pixel occupancy by dark counts $\text{DCR} \cdot \tau_r / N_{\text{pix}} \lesssim 0.2$, the response is close to linear and independent of the arrival time of the photons. If this is not the case and the probability of two or more Geiger discharges in a pixel during the time interval τ_r is significant, the response becomes non-linear and dependent on the arrival-time distribution of the photons and the readout electronics. In this case a quantitative understanding of the response and its parametrisation based on a physical model is complicated. So far, in the author's opinion, the situation is not fully understood, however as discussed in Ref. [14], for a given situation, the response function can be measured, and phenomenological parameterisations found and used to correct for the non-linearity. The observation of an increase in the mean number of Geiger discharges, $\langle N_G \rangle$, as a function of N_γ beyond N_{pix} and the observation that the pulse shape changes with the number of Geiger discharges in a single pixel, may point a way towards extending the measurement capabilities of

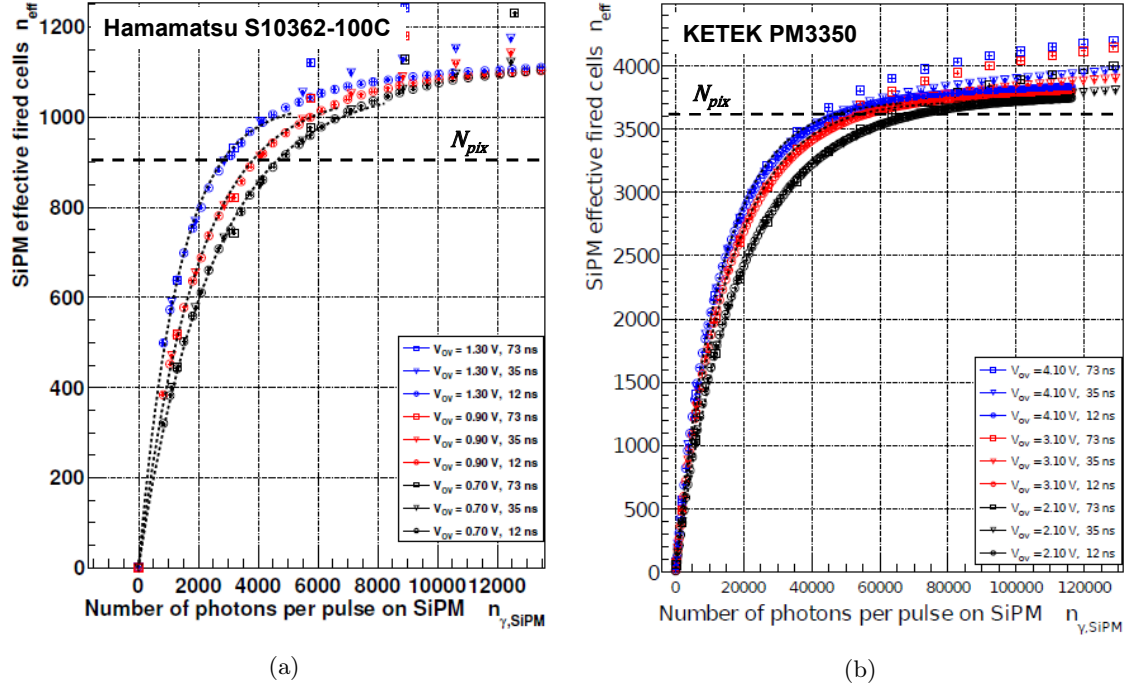


Figure 27: Effective number of Geiger discharges as a function of N_γ for (a) the Hamamatsu SiPM measured with a 150 ns gate, (b) the KETEK SiPM measured with a 400 ns gate from Ref. [14]. The insert gives the values of V_{OV} , and the duration of the light pulse.

SiPMs into the domain of high N_γ , where its response is highly non-linear. So far a detailed general study of the non-linearity and the worsening of the resolution caused by high pixel occupancies from dark counts caused by radiation damage, is also lacking. This is of particular relevance for the upgrade of the experiments at the Large Hadron Collider, LHC at CERN, where SiPMs will be exposed to high fluences of hadrons.

5. Conclusions and outlook

SiPMs have already found a broad range of applications, which is illustrated in the different contributions to this Special Issue of Nuclear Instruments and Methods devoted to SiPMs. Given the many new ideas for future applications, it is certain that the use of SiPMs will continue to expand. Well documented methods of characterisation, from which concise specifications can be derived, will become more and more important. The paper is an attempt to give an overview and clearly define the parameters required to describe the performance of SiPMs, discuss different characterisation methods, point out some of their limitations and give a number of recommendations.

The main aims of the efforts on SiPM characterisation are:

1. Provide a basis for specifications by the vendors, which allow users to choose the SiPM best suited for the intended application.
2. Enable quality control and sample selection.
3. Provide a basis for the development of the calibration and analysis methods for a given application.
4. Improve the basic understanding of SiPMs, which is the input for further improving their performance.

The characterisation methods which can be successfully used depend on the application regime, which are grouped in four classes:

1. *Low light level, temperature range -30°C to $+30^{\circ}\text{C}$, no radiation damage, no ambient light:* In these conditions pulses from 0, 1, 2, etc. Geiger discharges can be separated. From spectra recorded in the dark and with pulsed light, recorded either by a QDC, by integrating the current transient or by measuring the pulse amplitude after pulse-shaping, DCR (dark count rate), G^* (gain), V_{off} (turn-off voltage), relative PDE (photon-detection efficiency), ECF (excess charge factor) and ENF (excess noise factor) can be determined. Various methods are described in the paper. The measurements should be done as a function of V_{bias} (bias voltage) and for a few temperatures. The wavelength of the pulsed light source should be close to the wavelength relevant for the application. If necessary, the absolute PDE should be measured, which however is quite involved. In our view no detailed analysis of correlated pulses is required for most applications. The knowledge of ECF is sufficient to obtain the absolute number of photons producing primary Geiger discharges, and the optimum operating point with respect to photon resolution can be obtained from DCR , ECF and ENF . If the intention is to operate the SiPM at high over-voltages, the dark current, I_{dark} , as a function of V_{bias} should be investigated. It is not recommended to use the SiPM at V_{bias} values at which the slope of $\ln(I_{dark})$ shows a second increase.
2. *Like 1., however for cryogenic temperatures:* Given the large interest to use SiPMs at cryogenic temperatures in Dark Matter, neutrino-less double beta decay and neutrino oscillation experiments (Ref. [49]) significant efforts are devoted to developing and characterising SiPMs, which work at temperatures down to 100 K and even lower. At these low temperatures many properties of doped silicon change significantly compared to room temperature. This has a major impact on their performance, as discussed in Ref. [50]. The methods used so far are similar to those at higher temperatures. An example is Ref. [43, 51].
3. *Similar to 1., however for high light intensities:* In addition to the calibration suggested in 1., spectra should be recorded at high photon numbers, N_{γ} , and both mean values, $\langle Q \rangle$, and rms-spread, σ_Q , determined. The relative number of photons is obtained from a linear photon-detector, e.g. a photo-diode looking at the light source. The normalisation is obtained at low light intensities, where the SiPM is expected to be linear, from $N_{\gamma}^{norm} = \langle N_{pG} \rangle$ using $\langle N_{pG} \rangle$ from Eq. 3. In this way the calibration curve, $Q(N_{\gamma}^{norm})$, is obtained, which can be used to correct the measured Q for the non-linearity. As the non-linearity depends on the arrival time of the photons, it is important that the pulse shape of the calibration pulse is similar to the pulse shape of the intended application. To a lesser extent, the non-linearity also depends on the wavelength. Therefore the wavelength used for the calibration should be similar to the one of the intended application.
4. *High dark count rate due to radiation damage or ambient light:* If possible, the characterisation described in 1. should be performed in a situation, where the DCR is low, e.g. before irradiation. In addition, the dark current, I_{dark} , and the current with DC-light, I_{light} , should be measured as a function of V_{bias} . The comparison of $I_{photo} = I_{light} - I_{dark}$ for the low and high DCR situation already gives a good idea on the possible reduction of PDE due to high pixel occupancy by dark counts. Methods of how to determine DCR from I_{dark} , and how from σ_{dark} (spread of the recorded spectrum without illumination) are presented in the paper. The method using I_{dark} appears to be the more reliable one. In addition, a method of how to determine the relative PDE and G^* from the mean, $\langle Q \rangle$, and rms-spread, σ_Q of the spectrum with illumination in the absence of saturation effects, is presented. An extension of this method including saturation effects, which is relevant at high DCR values or high light intensity, still has to be developed.

In spite of large and highly successful efforts to characterise SiPMs, a lot of work remains to be done: Examples are the characterisation at cryogenic temperatures, the determination of the non-linearities at high photon intensities and the improvement of the measurement and analysis methods of highly radiation-damaged SiPMs.

6. Appendix

In this appendix Eq. 23, the relation between the variance, σ_{dark}^2 , and the primary dark count rate, DCR_p , for current pulses $I(t) = (q_0 \cdot G/\tau) \cdot e^{-t/\tau}$ occurring randomly at the rate DCR_p and integrated in the time interval t_{gate} , including the effects of correlated noise is derived. First, a single (1) SiPM pulse occurring at $t = 0$ is considered, with the current transient

$$I_1(t) = \begin{cases} 0 & \text{for } t < 0, \\ f(t) = \frac{1}{\tau} \cdot e^{-t/\tau} & \text{for } t \geq 0. \end{cases} \quad (26)$$

The integral Q_1 of the current for a gate starting at $t = t_1$ with width t_{gate} is

$$Q_1(t_1) = \begin{cases} 0 & \text{for } t_1 < -t_{gate}, \\ \int_0^{t_{gate}+t_1} f(t) dt = 1 - e^{-(t_{gate}+t_1)/\tau} & \text{for } -t_{gate} \leq t_1 < 0, \\ \int_{t_1}^{t_{gate}+t_1} f(t) dt = e^{-t_1/\tau}(1 - e^{-t_{gate}/\tau}) & \text{for } t_1 \geq 0. \end{cases} \quad (27)$$

Next, the mean charge $\langle Q_1(\Delta t_1) \rangle$ and the variance $\sigma_1^2(\Delta t_1) = \langle (Q(t_1) - \langle Q_1(\Delta t_1) \rangle)^2 \rangle$ for the t_1 interval from $-t_{gate}$ to t_0 , denoted $\Delta t_1 = t_{gate} + t_0$, are calculated. The value of t_0 is not relevant, as only the limes $\Delta t_1 \rightarrow \infty$ is relevant. One finds

$$\langle Q_1(\Delta t_1) \rangle = \lim_{\Delta t_1 \rightarrow \infty} \frac{\int_{\Delta t_1} Q(t_1) dt_1}{\Delta t_1} = \lim_{\Delta t_1 \rightarrow \infty} \frac{t_{gate} + \tau e^{-t_0/\tau} (e^{-t_{gate}/\tau} - 1)}{\Delta t_1} = \frac{t_{gate}}{\Delta t_1} \quad (28)$$

For the variance a similar calculation gives

$$\sigma_1^2(\Delta t_1) = \lim_{\Delta t_1 \rightarrow \infty} \frac{\int_{\Delta t_1} (Q(t_1) - \langle Q_1(\Delta t_1) \rangle)^2 dt_1}{\Delta t_1} = \frac{t_{gate} - \tau (1 - e^{-t_{gate}/\tau})}{\Delta t_1}. \quad (29)$$

For the dark count rate DCR_p , there will be on average $N_{DC} = DCR_p \cdot \Delta t_1$ dark counts in the time interval Δt_1 , and the pulse height distribution will be the convolution of N_{DC} single pulses with the mean

$$N_{DC} \cdot \langle Q_1 \rangle = DCR_p \cdot t_{gate}, \quad (30)$$

and the variance

$$N_{DC} \cdot \sigma_1^2 = DCR_p \cdot (t_{gate} - \tau \cdot (1 - e^{-t_{gate}/\tau})). \quad (31)$$

For finite Δt_1 values one has to take into account that N_{DC} is distributed according to a Poisson distribution, however in the limit $\Delta t_1 \rightarrow \infty$ the Poisson distribution approaches a δ -function at N_{DC} and its contribution to the variance vanishes.

Eq. 31 describes the variance for $q_0 \cdot G = 1$ in the absence of correlated noise from cross-talk and after-pulses. The effect of *ECF* and *ENF* is taken into account by replacing $\langle N_{pe} \rangle$ in Eq. 18 by $N_{DC} \cdot \sigma_1^2$ from Eq. 31, from which Eq. 23

$$\sigma_{dark}^2 = ((q_0 \cdot G)^2 \cdot ENF \cdot ECF^2 \cdot DCR_p) \cdot (t_{gate} - \tau \cdot (1 - e^{-t_{gate}/\tau})) \quad (32)$$

is obtained. For $t_{gate} \gg \tau$ the term in the right parenthesis is $\approx t_{gate} - \tau$, and for $t_{gate} \ll \tau$ it is $\approx t_{gate}^2/2\tau$.

Acknowledgement

I am grateful to the reviewers, who made many suggestions and thereby helped to improve the quality of the paper. I also want to thank the members of the Hamburg Detector Laboratory working on SiPMs for the measurements they performed, some of which are discussed in this paper, and for many comments and fruitful discussions.

7. List of References

References

- [1] International Conference on the Advancements of Silicon Photomultipliers, Schwetzingen 11.6.2018–15.6.2018, <http://icasipm.org>.
- [2] C. Piemonte and A. Gola, *Overview on the main parameters and technology of Silicon Photomultipliers*, this Special Issue on SiPMs.
- [3] F. Acerbi and S. Gundacker, *Understanding and simulating SiPMs*, this Special Issue on SiPMs.
- [4] P. P. Calo, F. Cicierello, C. Marzocca and S. Petrognani, *SiPM Readout Electronics*, this Special Issue on SiPMs.
- [5] F. Simon, *Silicon Photomultipliers in Particle and Nuclear Physics*, this Special Issue on SiPMs.
- [6] R. J. McIntyre, *On the Avalanche Initiation Probability of Avalanche Diodes Above the Breakdown Voltage*, IEEE-Transactions of Electron Devices 20(7), July 1973, 637–641.
- [7] V. Chmill et al., *Study of the breakdown voltage of SiPMs*, Nuclear Instruments and Methods in Physics Research A 645 (2017) 56.
- [8] O. Marinov, J. Dean and J. A. Jimenez Tejada, *Theory of microplasma fluctuations and noise in silicon diode in avalanche breakdown*, Journal of Applied Physics 101 (2007) 064515.
- [9] F. Corsi et al., *Electrical Characterisation of Silicon Photo-Multiplier Detectors for Optimal Front-End Design*, 2006 IEEE Nuclear Science Symposium Conference Record, 1276–1280.
- [10] C. Piemonte et al., *Characterization of the first Prototypes of Silicon Photomultiplier fabricated at ITC-irst*, IEEE Transactions on Nuclear Science Vol. 54(1), February 2007, 236–244.
- [11] V. Chmill et al., *On the characterisation of SiPMs from pulse-height spectra*, Nuclear Instruments and Methods in Physics Research Section A 854 (2017) 70–81.
- [12] S. Vinogradov, *Analytical models of probability distribution and excess noise factor of solid state photomultiplier signals with crosstalk*, Nuclear Instruments and Methods in Physics Research Section A 695 (2012) 247–251.
- [13] C. Piemonte et al., *Development of an automatic procedure for the characterization of silicon photomultipliers*, 2012 IEEE Nuclear Science Symposium and Medical Imaging Conference Record (NSS/MIC) N1-206, 428–432.
- [14] T. Bretz et al., *Dynamic range measurement and calibration of SiPMs*, Journal of Instrumentation, 2016 JINST 11 P03009.
- [15] E. Garutti and Yu. Musienko, *Radiation damage of SiPMs*, this Special Issue on SiPMs.
- [16] S. Seifert et al., *Simulation of Silicon Photomultiplier Signals*, IEEE Transactions on Nuclear Science Vol. 56(6) (2009) 3726–3733.
- [17] D. Marano et al., *Silicon Photomultipliers Electrical Model – Extensive Analytical Analysis*, IEEE Transactions on Nuclear Science Vol. 61(1) (2014) 23–34.
- [18] J. Rosado and S. Hidalgo, *Characterisation and modeling of crosstalk and afterpulsing in Hamamatsu silicon photomultipliers*, Journal of Instrumentation, 2015 JINST 1 P10031.
- [19] A. N. Otte, D. Garcia, T. Nguyen and D. Purshotam, *Characterisation of three high-efficiency and blue-sensitive silicon photomultipliers*, Nuclear Instruments and Methods in Physics Research A 864 (2017) 106–125.

- [20] M. Dziewiecki et al., *A system for automated measurement of parameters of large quantities of MPPC detectors*, International Workshop on New Photon Detectors (PD09), June 2009, Matsumoto, PoS(PD09)016.
- [21] P. Eckert et al., *Characterisation Studies of Silicon Photomultipliers*, Nuclear Instruments and Methods in Physics Research A 620 (2010) 217–226.
- [22] F. Barbosa et al., *Silicon photomultiplier characterization for the GlueX barrel calorimeter*, Nuclear Instruments and Methods in Physics Research A 695 (2012) 10–14.
- [23] Chen Xu, *Study of the Silicon Photomultipliers and their Application in Positron Emission Tomography*, PhD Thesis, University of Hamburg, May 2014, DESY-THESIS-14-0013.
- [24] V. Arosio et al., *An Educational Kit Based on a Modular Silicon Photomultiplier System*, arXiv:1308.3622v2.
- [25] A. N. Otte et al., *A measurement of the photon detection efficiency of silicon photomultipliers*, Nuclear Instruments and Methods in Physics Research A 567 (2006) 360–363.
- [26] G. Bonanno et al., *Precision measurements of Photon Detection Efficiency for SiPM detectors*, Nuclear Instruments and Methods in Physics Research A 610 (2016) 93–97.
- [27] Wang Yue et al., *Performance of ultra-small silicon photomultiplier array with active area of $0.12\text{ mm} \times 0.12\text{ mm}$* , Nuclear Instruments and Methods in Physics Research A 787 (2015) 38–41.
- [28] Seul Ji Yang, et al., *Precision measurement of the photon detection efficiency of silicon photomultipliers using two integrating spheres*, Optics Express, Vol. 2 (1) (2014) 716–721.
- [29] M. López, H. Hofer and S. Kück, *Detection efficiency calibration of single-photon silicon avalanche photodiodes traceable using double attenuator technique*, Journal of Modern Optics, Vol. 62 (S2) (2015) S21–S27.
- [30] E. Garutti, M. Gensch, R. Klanner, M. Ramilli and C. Xu, *Afterpulse effect in SiPM and neutron irradiation studies*, 2014 IEEE Nuclear Science Symposium and Medical Imaging Conference (NSS/MIC), Seattle, 2014.
- [31] Eugen Engelmann, *Dark-count rate of silicon photomultipliers – Meteorological characterisation and suppression*, PhD Thesis, Universität der Bundeswehr München, May 2018.
- [32] R. Newman, *Visible light from a silicon pn junction*, Phys. Rev. 100 (1955) 700–703.
- [33] A. L. Lacaita, F. Zappa, S. Bigliardi and M. Manfredi, *On the Bremsstrahlung Origin of Hot-Carrier-Induced Photons in Silicon Devices*, IEEE Transactions on Electron Devices 40(3) (1993) 577–582.
- [34] R. Mirzoyan, R. Kosyra and H.-G. Moser, *Light emission in Si avalanches*, Nuclear Instruments and Methods in Physics Research A 610 (2009) 98–100.
- [35] T. Frach et al., *The digital silicon photomultiplier – Principle of operation and intrinsic detector performance*, 2009 IEEE Nuclear Science Symposium Conference Record (NSS/MIC) 1959–1965.
- [36] C. Xu, R. Klanner, E. Garutti and W.-D. Hellweg, *Influence of X-ray irradiation on the properties of the Hamamatsu silicon photomultiplier S10362-11-050C*, Nuclear Instruments and Methods in Physics Research A 762 (2014) 149–161.
- [37] M. Centis Vignali et al., *Neutron irradiation effect on SiPMs up to $\Phi_{neq} = 5 \times 10^{14}\text{ cm}^{-2}$* , arXiv:1709.04648.

- [38] A.S. Grove, *Physics and Technology of Semiconductor Devices*, 1967, John Wiley & Sons.
- [39] A. Otte, T. Nguyen and J. Stansbury, *Locating the avalanche structure and the origin of breakdown generating charge carriers in silicon photomultipliers by using the bias dependent breakdown probability*, subm. to Nuclear Instruments and Methods in Physics Research (2018).
- [40] M. Gaug, H. Bartko, J. Cortina and J. Rico, *Calibration of the MAGIC Telescope*, Proceedings of the 29-th International Cosmic Ray Conference, Pune (2005) 101–106.
- [41] Y. Du and F. Retière, *After-pulsing and cross-talk in multi-pixel photon counters*, Nuclear Instruments and Methods in Physics Research Section A 596 (2005) 396–401.
- [42] F. Acerbi et al., *NUV Silicon Photomultipliers With High Detection Efficiency and Reduced Delayed Correlated-Noise*, IEEE Transactions on Nuclear Science 62(3) (2015) 1318–1325.
- [43] F. Acerbi et al., *Cryogenic Characterization of FBK HD Near-UV Sensitive SiPMs*, IEEE Transactions on Electron Devices Vol. 64(2), February 2017, 521–526.
- [44] R. Klanner, *Characterisation of radiation-damaged SiPMs*, Talk presented at ICASiPM, Schwetzingen, 11.6.2018–15.6.2018, [1].
- [45] L. Gruber, S. E. Brunner, J. Marton and K. Suzuki, *Over saturation behavior of SiPMs at high photon exposure*, Nuclear Instruments and Methods in Physics Research Section A 737 (2014) 11–18.
- [46] E. Popova, *Physics and Experimental Study of SiPM Nonlinearity and Saturation* Talk presented at ICASiPM, Schwetzingen, 11.6.2018–15.6.2018, [1].
- [47] Q. Weitzel et al., *Measurement of the Response of Silicon Photomultipliers from Single Photon Detection to Saturation*, presented at PM2018, the 14th Pisa Meeting on Advanced Detectors, La Biodola, May 27 to June 2, 2018, <https://agenda.infn.it/event/PM2018>.
- [48] S. Krause, *A Method and Experimental SetUp to Measure SiPM Saturation*, Talk presented at ICASiPM, Schwetzingen, 11.6.2018–15.6.2018, [1].
- [49] F. Retière, *Cryogenic applications of SiPMs*, Talk presented at ICASiPM, Schwetzingen, 11.6.2018–15.6.2018, [1].
- [50] G. Collazuol, M. G. Bisogni, S. Marcatili, C. Piemonte, and A. Del Guerra, *Studies of silicon photomultipliers at cryogenic temperatures*, Nuclear Instruments and Methods in Physics Research Section A 628 (2011) 389–392.
- [51] C. E. Aalseth et al., *Cryogenic Characterization of FBK RGB-HD SiPMs*, Journal of Instrumentation, JINST 12 (2017) P09030, and arXiv:1705.07028.